This is the post-print, accepted manuscript in the *AIAA Journal of Aerospace Information Systems*: "A tutorial review of indirect wind estimation methods using small uncrewed air vehicles," Z. Ahmed, M. H. Halefom, and C. A. Woolsey. *AIAA J. Aerospace Information Systems*. 21(8), pp. 667-683 [DOI: 10.2514/1.I011345]

A Tutorial Review of Indirect Wind Estimation Methods Using Small Uncrewed Air Vehicles

Zakia Ahmed *, Mekonen H. Halefom†, and Craig Woolsey‡
Virginia Polytechnic Institute and State University, Blacksburg, Virginia 24061

I. Introduction

Small uncrewed air vehicles (UAVs) are used for a number of applications including package delivery [1], infrastructure inspection [2], crop monitoring and smart spraying [3], and terrain mapping [4]. Another compelling application is atmospheric sensing [5–9]. A UAV might be used, for example, to measure the thermodynamic state (pressure, temperature, and humidity, or PTH) and the kinematic state (wind velocity) of the atmospheric boundary layer (ABL). Using UAVs to sample the ABL can aid numerical weather prediction and help scientists understand climatological or topological phenomena such as variations in flow over complex terrain [6, 8, 10]. UAVs have also been used to measure wind in the wake of a marine vessel to validate computational fluid dynamics (CFD) models [11–16]. Additionally, wind field estimates can be incorporated into flight path planning and control [17], and the wind may even be exploited to improve energy efficiency [18–20]. The urban air mobility (UAM) concept [21], where small aircraft take off and land at urban vertiports, increases the need for accurate, real-time wind field measurements to support safe, reliable flight.

While UAV-based measurements of atmospheric properties like PTH involve direct sampling using dedicated onboard sensors, wind inference methods may involve either direct or indirect measurements. Direct measurements are taken with multihole pressure probes, for example, or sonic anemometers that are mounted on a UAV [22]. Indirect measurements are obtained by inferring wind velocity from the disturbed (*i.e.*, uncommanded) aircraft motion caused by the ambient wind. Considerations for direct measurements are the cost and accuracy of the sensors and their placement on the UAV so that, for example, the aircraft's propulsion system does not corrupt the measurements. Indirect measurements are the focus of this survey. They are computed using standard operational sensors, such as the inertial measurement unit (IMU) and a global navigation satellite system (GNSS) receiver, thus adding no additional cost, weight, or complexity to the aircraft.

*Ph.D. Student, Mechanical Engineering, AIAA Student Member, Email: zakiaahmed@vt.edu
†Ph.D. Candidate, Kevin T. Crofton Department of Aerospace and Ocean Engineering, AIAA Student Member, Email: hmeko13@vt.edu
‡Professor, Kevin T. Crofton Department of Aerospace and Ocean Engineering, AIAA Associate Fellow, Email: cwoolsey@vt.edu

As described above, indirect wind measurement methods use the aircraft as the wind sensor as opposed to direct wind estimation where an aircraft is equipped with a dedicated wind sensor. Indirect wind estimation methods can be further categorized as model-based, model-free, or a combination of the two. Model-based wind estimation uses aircraft operational sensor measurements fused with the aircraft dynamic model to determine wind velocity. In contrast, model-free methods use only the operational sensor suite without knowledge of the aircraft dynamic model to compute estimates of the wind. Model-free methods may require an aircraft to execute specific maneuvers to obtain wind estimates whereas model-based wind estimation methods typically do not impose restrictions on the flight path. Different estimation approaches can be used with the model-based or model-free methods including linear or nonlinear observers and machine learning methods. Machine learning methods require direct wind measurements in order to train the estimation algorithm. This paper is focused on approaches that do not require direct wind measurements, either before or during wind estimation, except for the purpose of validating results. Specifically, this paper focuses on the use of deterministic (Luenberger) observers, Kalman filters (KFs), extended Kalman filters (EKFs), and unscented Kalman filters (UKFs) for wind estimation.

Existing surveys on wind sensing are concerned with wind field representation, onboard sensors, and fixed-wing UAV motion in wind [23] or on direct measurements and tilt-angle-based wind sensing using multirotor UAVs [24]. While [23] and [24] discuss indirect wind estimation, specific wind estimation algorithms are not explored in detail. This survey is intended to provide a comprehensive review of indirect wind estimation using both types of small UAV, including a discussion of common algorithms. The paper describes the wind field and various wind field assumptions, summarizes the aircraft equations of motion in wind noting differences between the equations for fixed-wing and multirotor UAVs, describes four common state estimation approaches, reviews indirect wind inference methods making a distinction between model-based and model-free methods, and describes the implementation of the KF, EKF, and UKF schemes for simulated flight in wind of a small, fixed-wing UAV. The focus on estimators and their implementation clearly illustrates how assumptions about the wind field, the aircraft equations of motion, and different estimation schemes affect wind estimates. A comparison of the filters exposes some implementation challenges and illustrates differences in estimation accuracy.

The paper is organized as follows. Models for flight in wind are described in Section II. The dynamic equations of an aircraft including wind disturbances are given in Section III. A summary of the different filters used in wind estimation schemes is provided in Section IV. A description of existing work on wind estimation methods separated into model-based and model-free methods is presented in Section V. Implementation of model-based wind estimation for a simulated fixed-wing UAV subject to two-dimensional von Kármán turbulence, using a KF, EKF, and UKF, is described in Section VI. Conclusions and suggestions for continuing work are presented in Section VII.

II. Description of the Wind Field

Wind estimation schemes that use measurements obtained from UAVs are often informed by assumptions made about the wind field. For example, a model-based estimator might assume that the wind velocity is steady and uniform so that wind estimates are only updated based on measurements. Or the estimator might assume that the wind velocity varies as a random walk. Here, we describe some common assumptions about wind fields, which may inform the choice of wind model incorporated in the estimator. First, we review some standard reference frames that are used to describe wind and aircraft motion.

A. Reference Frames

Describing the wind field and related assumptions, and later defining an aircraft's motion in wind, first requires a definition of the relevant reference frames. In this paper, all reference frames are right-handed with mutually orthogonal axes. We consider four frames: the inertial, the earth-fixed, the body-fixed, and the atmosphere-fixed reference frames [25–27].

- The *inertial* reference frame is represented by the orthonormal triad $\{\boldsymbol{i}_x, \boldsymbol{i}_y, \boldsymbol{i}_z\}$. Its origin and orientation are arbitrary, but the frame does not accelerate relative to the distant stars, so Newton's laws of motion hold in this frame.
- The *earth-fixed* reference frame is represented by the orthonormal triad $\{\boldsymbol{e}_x, \boldsymbol{e}_y, \boldsymbol{e}_z\}$. The origin of the earth-fixed reference frame is located at an arbitrary (non-polar) point on Earth's surface, with the positive $\boldsymbol{e}_x$ axis pointing towards geographic north, the positive $\boldsymbol{e}_y$ axis pointing east, and the positive $\boldsymbol{e}_z$ axis pointing down, completing the orthonormal frame. In this case, the reference frame is called a North-East-Down (NED) frame. For flight mechanics applications, it is common to assume the earth reference frame is inertial. Because we consider wind velocity measurement over short time and space scales, we adopt that assumption here.
- The *body-fixed* reference frame, represented by the orthonormal triad $\{\boldsymbol{b}_x, \boldsymbol{b}_y, \boldsymbol{b}_z\}$, has its origin fixed at the aircraft's center of gravity. The positive $\boldsymbol{b}_x$ axis points towards the front of the vehicle (e.g., out the nose, for a fixed-wing aircraft), the positive $\boldsymbol{b}_y$ axis points to the right side, and the positive $\boldsymbol{b}_z$ axis points through the underside of the aircraft. We let $\boldsymbol{R}_{\mathrm{IB}}$ denote the proper rotation matrix that maps free vectors from the body-fixed frame to the earth-fixed frame (which we have taken to be inertial); transformations between these two frames are discussed in Section III.
- The *atmosphere-fixed* reference frame is represented by the orthonormal triad $\{\boldsymbol{a}_x, \boldsymbol{a}_y, \boldsymbol{a}_z\}$. When the atmosphere is, or is assumed to be, at rest relative to the Earth, then the earth-fixed and atmosphere-fixed frames are the same. If the atmosphere is in uniform motion with constant velocity relative to the earth-fixed frame, then the atmosphere-fixed frame moves relative to the earth-fixed frame with the same constant velocity.

B. Wind Velocity Vector Field

Wind velocity is modeled as a vector-valued random process. It can be decomposed into (i) a deterministic mean value that varies slowly in time and space and (ii) random time- and space-varying fluctuations from this mean value. Let $\boldsymbol{W}(\boldsymbol{P}, t)$ denote the wind field at the inertial position $\boldsymbol{P} = [x, y, z]^{\mathrm{T}}$ and time t. Then

$$\boldsymbol{W}(\boldsymbol{P}, t) = \bar{\boldsymbol{W}}(\boldsymbol{P}, t) + \tilde{\boldsymbol{W}}(\boldsymbol{P}, t) \tag{1}$$

where $\bar{\boldsymbol{W}}(\boldsymbol{P}, t)$ is the slow varying deterministic mean wind velocity vector and $\tilde{\boldsymbol{W}}(\boldsymbol{P}, t) = [\tilde{W}_x, \tilde{W}_y, \tilde{W}_z]^{\mathrm{T}}$ is the random fluctuation.

Associated with any given point $\boldsymbol{P}$ and time t, there is a 3×3 correlation matrix $\boldsymbol{R}(\boldsymbol{P}, t, \boldsymbol{\zeta}, \tau)$ defined as the ensemble average of the outer product of $\tilde{\boldsymbol{W}}(\boldsymbol{P}, t)$ with $\tilde{\boldsymbol{W}}(\boldsymbol{P} + \boldsymbol{\zeta}, t + \tau)$, where $\boldsymbol{\zeta}$ and τ are the spatial and temporal correlation variables, respectively. The components of the correlation matrix are

$$R_{ij}(\boldsymbol{P}, t, \boldsymbol{\zeta}, \tau) = < \tilde{W}_i(\boldsymbol{P}, t)\tilde{W}_j(\boldsymbol{P} + \boldsymbol{\zeta}, t + \tau) > \tag{2}$$

for $i, j \in \{x, y, z\}$, where $< \cdot, \cdot >$ denotes the ensemble average.

The component functions R_{ij} provide an incomplete description of the wind turbulence, modeled as a random process, but it is common to characterize turbulence using the information contained in R_{ij}. The functional form of these component functions and the corresponding parameter values depend on meteorological conditions, terrain, and other factors. Atmospheric turbulence is often well characterized by one or more of the following assumptions [26, Ch. 13].

Assumption 1 *Common Assumptions Concerning Atmospheric Turbulence*

a) *The joint probability density functions underlying the correlation functions (2) are Gaussian.*

b) *The process is stationary: R_{ij} does not depend on time t for $i, j \in \{x, y, z\}$.*

c) *The process is homogeneous: R_{ij} does not depend on position $\boldsymbol{P}$ for $i, j \in \{x, y, z\}$.*

d) *The process is isotropic: R_{ij} does not depend on the orientation of the frame in which the wind vector is defined. Equivalently, the mean-square velocity components are equal in every direction: $\langle \tilde{W}_x^2 \rangle = \langle \tilde{W}_y^2 \rangle = \langle \tilde{W}_z^2 \rangle = \sigma^2$.*

At low altitudes, atmospheric turbulence varies with height, thus Assumption 1d does not hold. The rate of change of the wind velocity as seen by a particle moving along a trajectory $\boldsymbol{P}(t)$ is

$$\frac{d}{dt}\boldsymbol{W}(\boldsymbol{P}, t) = \left(\frac{\partial}{\partial t}\bar{\boldsymbol{W}}(\boldsymbol{P}, t) + \nabla\bar{\boldsymbol{W}}(\boldsymbol{P}, \boldsymbol{t}) \cdot \frac{d\boldsymbol{P}}{dt}\right) + \left(\frac{\partial}{\partial t}\tilde{\boldsymbol{W}}(\boldsymbol{P}, t) + \nabla\tilde{\boldsymbol{W}}(\boldsymbol{P}, t) \cdot \frac{d\boldsymbol{P}}{dt}\right) \tag{3}$$

where ∇ denotes the gradient with respect to three-dimensional position.

The nature of the aircraft's flight can produce additional simplifications to Eq. (3). For fixed-wing aircraft flying straight and level at a constant altitude and speed, the position of the aircraft typically changes much faster than the spatial profile of the velocity fluctuations. In this case, the turbulent fluctuations can be treated as a frozen pattern advecting with the mean wind velocity $\bar{\boldsymbol{W}}$ [26, Ch. 13]. This assumption is referred to as Taylor's frozen turbulence hypothesis. Kaimal and Finnigan remark that Taylor's hypothesis can be adopted for any *in situ* sensor as it is assumed that the turbulent eddies "change imperceptibly" as they are convected by the mean wind past the sensor [28, pg. 33]. While turbulence is neither frozen nor transported at mean wind speeds, the lifetime of an eddy is long compared to the travel time across a sensor. Experimental investigations find good agreement between atmospheric measurements made with moving and stationary probes when it is assumed that eddies are convected by the mean wind without deforming. Thus, Taylor's hypothesis can be adopted for static or slowly moving objects, such as a hovering rotary-wing aircraft, as well as for fixed-wing airplanes in fast, forward flight through turbulence. Summarizing these points, one may adopt one or more of the following assumptions.

Assumption 2 *Steady Mean Wind, Uniform Mean Wind, and Frozen Turbulence*

a) *The mean wind velocity does not vary with time:* $\frac{\partial}{\partial t}\bar{\boldsymbol{W}}(\boldsymbol{P},t) = \boldsymbol{0}$*, thus* $\bar{\boldsymbol{W}}(\boldsymbol{P},t) = \bar{\boldsymbol{W}}(\boldsymbol{P})$.

b) *The mean wind velocity does not vary with position:* $\nabla\bar{\boldsymbol{W}}(\boldsymbol{P},t) = \boldsymbol{0}$*, thus* $\bar{\boldsymbol{W}}(\boldsymbol{P},t) = \bar{\boldsymbol{W}}(t)$.

c) *(Taylor's hypothesis.) Random fluctuations from the mean wind velocity vary only in space:* $\frac{\partial}{\partial t}\tilde{\boldsymbol{W}}(\boldsymbol{P},t) = \boldsymbol{0}$*, so that* $\tilde{\boldsymbol{W}}(\boldsymbol{P},t) = \tilde{\boldsymbol{W}}(\boldsymbol{P})$.

Assumptions 2a and 2b together imply that $\bar{\boldsymbol{W}}$ is a constant vector. In reality, the mean wind will always vary over a flight. If one adopts a steady, uniform flow model for the wind estimation problem, these variations must be captured by measurement updates in the model-based estimator. More commonly in wind estimation, the dynamics of the total wind velocity are assumed to be driven by Gaussian white noise. For the case characterized by Assumption 2, one has

$$\frac{d}{dt}\boldsymbol{W}(\boldsymbol{P},t) = \frac{d}{dt}\left(\bar{\boldsymbol{W}} + \tilde{\boldsymbol{W}}(\boldsymbol{P})\right) = \nabla\tilde{\boldsymbol{W}}(\boldsymbol{P})\dot{\boldsymbol{P}} = \tilde{\boldsymbol{w}}_W \tag{4}$$

where the stochastic wind velocity fluctuation $\tilde{\boldsymbol{W}}$ is assumed to be a Wiener process whose generalized derivative $\tilde{\boldsymbol{w}}_W$ is continuous-time white noise [29, Ch. 3]. In other words, the perturbations in wind velocity from its steady, uniform mean value are modeled as a random-walk process. Note that $\tilde{\boldsymbol{w}}_W$ captures the combined effect of the variability in the frozen turbulence field and the velocity of the aircraft through that flow field. The model (4) is a commonly used representation of fluctuations from a constant, uniform mean wind, though a given wind estimation algorithm may or may not incorporate this representation.

III. Aircraft Equations of Motion in Wind

The dynamic equations for an aircraft in wind are presented here, together with assumptions about the aircraft and its motion. The following assumptions are common in formulating an aircraft flight dynamic model [26, 30]:

Assumption 3 *Rigid Body Equations of Motion in Wind*

a) *The aircraft mass is constant.*

b) *The aircraft is a rigid body.*

c) *The surface of the Earth is flat.*

d) *The specific force of gravity is constant.*

e) *The Earth is fixed in inertial space.*

Assumption 3e implies that the inertial and earth-fixed frames are equivalent. The aircraft's inertial position in the NED frame is denoted $\boldsymbol{P} = [P_x, P_y, P_z]^{\mathrm{T}}$. Its orientation can be described using conventional roll-pitch-yaw Euler angles $\boldsymbol{\Theta} = [\phi, \theta, \psi]^{\mathrm{T}}$. In terms of these angles, the rotation matrix that maps free vectors from the body-fixed frame to the inertial frame is

$$\boldsymbol{R}_{\mathrm{IB}} = \begin{pmatrix} \cos\theta\cos\psi & \cos\psi\sin\theta\sin\phi - \cos\phi\sin\psi & \cos\psi\sin\theta\cos\phi + \sin\phi\sin\psi \\ \cos\theta\sin\psi & \sin\phi\sin\theta\sin\psi + \cos\phi\cos\psi & \sin\theta\cos\phi\sin\psi - \sin\phi\cos\psi \\ -\sin\theta & \cos\theta\sin\phi & \cos\theta\cos\phi \end{pmatrix} \tag{5}$$

The matrix $\boldsymbol{R}_{\mathrm{BI}}$ mapping free vectors from the inertial frame to the body frame is $\boldsymbol{R}_{\mathrm{BI}} = \boldsymbol{R}_{\mathrm{IB}}^{-1} = \boldsymbol{R}_{\mathrm{IB}}^{\mathrm{T}}$. The matrix $\boldsymbol{L}_{\mathrm{IB}}(\boldsymbol{\Theta})$, which relates the body angular velocity vector $\boldsymbol{\omega}$ to the aircraft's attitude rate vector $\dot{\boldsymbol{\Theta}}$ in Eq. (10b) below, is

$$\boldsymbol{L}_{\mathrm{IB}} = \begin{pmatrix} 1 & \sin\phi\tan\theta & \cos\phi\tan\theta \\ 0 & \cos\phi & -\sin\phi \\ 0 & \sin\phi\sec\theta & \cos\phi\sec\theta \end{pmatrix} \tag{6}$$

The velocity of the aircraft with respect to the inertial frame can be written as the vector sum of the vehicle's air-relative velocity and the wind velocity. The angular velocity vector may be decomposed similarly. Writing these vectors in the body frame, we have:

$$\boldsymbol{v} = \boldsymbol{v}_{\mathrm{r}} + \boldsymbol{R}_{\mathrm{IB}}^{\mathrm{T}}\boldsymbol{V}_{\mathrm{w}} \tag{7a}$$

$$\boldsymbol{\omega} = \boldsymbol{\omega}_{\mathrm{r}} + \boldsymbol{\omega}_{\mathrm{w}} \tag{7b}$$

where $\boldsymbol{v} = [u, v, w]^{\mathrm{T}}$ and $\boldsymbol{\omega} = [p, q, r]^{\mathrm{T}}$ are the linear and angular velocity, respectively, $\boldsymbol{v}_{\mathrm{r}} = [u_{\mathrm{r}}, v_{\mathrm{r}}, w_{\mathrm{r}}]^{\mathrm{T}}$ and

$\boldsymbol{\omega}_\mathrm{r} = [p_\mathrm{r}, q_\mathrm{r}, r_\mathrm{r}]^\mathrm{T}$ are the air-relative linear and angular velocity, and $\boldsymbol{V}_\mathrm{w} = \boldsymbol{W}(\boldsymbol{P}, t) = [V_{\mathrm{w},x}, V_{\mathrm{w},y}, V_{\mathrm{w},z}]$ is the velocity of the wind expressed in the inertial frame at a given inertial position $\boldsymbol{P}$ of the aircraft and time t. The term $\boldsymbol{\omega}_\mathrm{w}$ merits further discussion.

The spatial gradient of the wind velocity along the trajectory of the aircraft can be expressed in the body-fixed frame of reference as follows:

$$\nabla \boldsymbol{v}_\mathrm{w} = \boldsymbol{R}_\mathrm{IB}^\mathrm{T} \nabla \boldsymbol{W} \boldsymbol{R}_\mathrm{IB} = \begin{bmatrix} \frac{\partial u_\mathrm{w}}{\partial x} & \frac{\partial u_\mathrm{w}}{\partial y} & \frac{\partial u_\mathrm{w}}{\partial z} \\ \frac{\partial v_\mathrm{w}}{\partial x} & \frac{\partial v_\mathrm{w}}{\partial y} & \frac{\partial v_\mathrm{w}}{\partial z} \\ \frac{\partial w_\mathrm{w}}{\partial x} & \frac{\partial w_\mathrm{w}}{\partial y} & \frac{\partial w_\mathrm{w}}{\partial z} \end{bmatrix} \tag{8}$$

where $\boldsymbol{v}_\mathrm{w} = [u_\mathrm{w}, v_\mathrm{w}, w_\mathrm{w}]^\mathrm{T}$ is the wind velocity vector expressed in the body-fixed reference frame and displacements x, y, and z are with respect to the body frame. The spatial gradient matrix in Eq. (8) can be decomposed into a symmetric part and a skew-symmetric part. The symmetric part represents dilation, which is typically ignored in engineering models of atmospheric turbulence, and especially in flight dynamics applications. The skew-symmetric part represents rotating flow, which results in an effective body angular rate $\boldsymbol{\omega}_\mathrm{w} = [p_\mathrm{w}, q_\mathrm{w}, r_\mathrm{w}]^\mathrm{T}$ felt by the aircraft. (Note that this flow nonuniformity may arise in the mean flow, the turbulent fluctuations, or both.) Because an aircraft has a physical size and shape, unlike a particle, one finds in practice that the rotational flow effect is dominated by certain aspects of the aircraft geometry. For a fixed-wing aircraft, for example, whose shape and scale are predominantly determined by the wing and fuselage, it is reasonable to take [31]

$$p_\mathrm{w} = -\frac{\partial w_\mathrm{w}}{\partial y} \qquad q_\mathrm{w} = \frac{\partial w_\mathrm{w}}{\partial x} \qquad r_\mathrm{w} = \frac{\partial v_\mathrm{w}}{\partial x} \tag{9}$$

The following system of equations approximates the motion of a rigid aircraft in wind [30]:

$$\dot{\boldsymbol{P}} = \boldsymbol{R}_\mathrm{IB} \boldsymbol{v} \tag{10a}$$

$$\dot{\boldsymbol{\Theta}} = \boldsymbol{L}_\mathrm{IB} \boldsymbol{\omega} \tag{10b}$$

$$\dot{\boldsymbol{v}} = \boldsymbol{v} \times \boldsymbol{\omega} + \frac{1}{m} \boldsymbol{F}_A(\dot{\boldsymbol{v}}_\mathrm{r}, \boldsymbol{v}_\mathrm{r}, \boldsymbol{\omega}_\mathrm{r}, \boldsymbol{\delta}) + \frac{1}{m} \boldsymbol{R}_\mathrm{IB}^\mathrm{T} \boldsymbol{F}_G \tag{10c}$$

$$\dot{\boldsymbol{\omega}} = \boldsymbol{I}^{-1} (\boldsymbol{I}\boldsymbol{\omega} \times \boldsymbol{\omega}) + \boldsymbol{I}^{-1} \boldsymbol{M}_A(\dot{\boldsymbol{v}}_\mathrm{r}, \boldsymbol{v}_\mathrm{r}, \boldsymbol{\omega}_\mathrm{r}, \boldsymbol{\delta}) \tag{10d}$$

where $\boldsymbol{F}_A = [X, Y, Z]^\mathrm{T}$ is the aerodynamic force vector including thrust and $\boldsymbol{M}_A = [L, M, N]^\mathrm{T}$ is the aerodynamic moment about the center of gravity, both expressed in the body-fixed frame. These aerodynamic terms depend on the air-relative velocity and angular velocity, as well as the control input vector $\boldsymbol{\delta}$. They may also depend on the air-relative acceleration, either through "added mass" effects [32] or, more typically, through quasisteady corrections for unsteady effects. (For fixed-wing aircraft, for example, it is common to incorporate a lift force and pitch moment due to plunge

acceleration.) Note that the inertial vector $\boldsymbol{F}_G = [0, 0, mg]^{\mathrm{T}}$ representing the aircraft weight is transformed to the body frame in Eqs. (10). The symmetric, positive definite matrix:

$$\boldsymbol{I} = \begin{pmatrix} I_{xx} & -I_{xy} & -I_{xz} \\ -I_{xy} & I_{yy} & -I_{yz} \\ -I_{xz} & -I_{yz} & I_{zz} \end{pmatrix}$$

is the matrix of moments of inertia computed in the body-fixed frame. For fixed-wing aircraft whose x-z plane is a plane of symmetry, $I_{xy} = I_{yz} = 0$. For multirotor aircraft, it is commonly assumed that $I_{xy} = I_{yz} = I_{xz} = 0$.

Equations (10) reflect approximations beyond those enumerated in Assumption 3. For example, Eq. (10c) omits a force due to flow nonuniformity; see Eq. (14) in [32]. Also, additional dynamic equations would be required to capture unsteady aerodynamics, should these effects play an important role [33, 34].

The aerodynamic force and moment models – i.e., the explicit expressions for $\boldsymbol{F}_A$ and $\boldsymbol{M}_A$ – are presented differently for fixed-wing and multirotor aircraft in standard references because of the fundamental differences in how motion is generated and controlled. For a fixed-wing aircraft, thrust is generated along the direction of the body x-axis. The resulting aerodynamic lift created by the wing supports the weight and effects turning motions through small adjustments in the aircraft attitude caused by control moment actuators (i.e., the control surfaces). For multirotor vehicles considered within the references cited in this paper, the propulsors generate thrust along the body z-axis, directly supporting both the aircraft weight and its translational motion through combined and differential thrust. For multirotor aircraft with canted rotor arms, the force generated along the rotor hub axis can be decomposed into components, one of which will act along the body z-axis. Aircraft that are capable of both rotary and fixed-wing flight – e.g., "lift-plus-cruise" aircraft – are capable of both horizontal and vertical propulsion and operate in three flight regimes: rotary, wing-borne, and transitional flight. The aerodynamic force and moment models for transitional flight may include elements from both rotary and wing-borne flight dynamic models.

For a fixed-wing aircraft, the aerodynamic force and moment are typically represented in non-dimensional form, to separate the effect of dynamic pressure and aircraft size and geometry from other force and moment dependencies. The aerodynamic force and moment coefficients are represented using dimensionless stability derivatives [30], which can be determined by applying model identification methods to flight test data [35–39].

For multirotor aircraft, the aerodynamic force and moment terms are often left in dimensional form. A detailed derivation of a multirotor aerodynamic force and moment model can be found in [40, 41], for example, where the rotor blades are considered to be rigid and rigidly fixed to the rotor hub. Aerodynamic force and moment models for multirotors and helicopters can include additional modes of blade motion such as flapping and coning, further complicating the flight dynamic model; a discussion of helicopter aerodynamics in wind can be found in [11], for

example.

IV. Estimators

The selection of an estimation algorithm is guided by aircraft model assumptions and computational considerations. This section reviews common model assumptions and estimator choices described in the literature about wind estimation using UAVs and identifies some advantages and disadvantages of these assumptions and choices.

A. Augmented Aircraft Equations of Motion in Wind

Model-based wind estimation requires a dynamic model for the aircraft motion and wind velocity. Here, we augment the nonlinear equations (10) with the wind model (4) and replace the total velocity $\boldsymbol{v}$ with Eq. (7a):

$$\dot{\boldsymbol{P}} = \boldsymbol{R}_{\mathrm{IB}}\boldsymbol{v}_{\boldsymbol{r}} + \boldsymbol{V}_{\mathrm{w}} \tag{11a}$$

$$\dot{\boldsymbol{\Theta}} = \boldsymbol{L}_{\mathrm{IB}}\boldsymbol{\omega} \tag{11b}$$

$$\dot{\boldsymbol{v}}_{\mathbf{r}} = \boldsymbol{v}_{\mathrm{r}} \times \boldsymbol{\omega} + \frac{1}{m}\boldsymbol{F}_A(\dot{\boldsymbol{v}}_{\mathrm{r}}, \boldsymbol{v}_{\mathrm{r}}, \boldsymbol{\omega}_{\mathrm{r}}, \boldsymbol{\delta}) + \frac{1}{m}\boldsymbol{R}_{\mathrm{IB}}^{\mathrm{T}}\boldsymbol{F}_G - \boldsymbol{R}_{\mathrm{IB}}^{\mathrm{T}}\tilde{\boldsymbol{w}}_{\mathrm{W}} \tag{11c}$$

$$\dot{\boldsymbol{\omega}} = \boldsymbol{I}^{-1}(\boldsymbol{I}\boldsymbol{\omega} \times \boldsymbol{\omega}) + \boldsymbol{I}^{-1}\boldsymbol{M}_A(\dot{\boldsymbol{v}}_{\mathrm{r}}, \boldsymbol{v}_{\mathrm{r}}, \boldsymbol{\omega}_{\mathrm{r}}, \boldsymbol{\delta}) \tag{11d}$$

$$\dot{\boldsymbol{V}}_{\mathrm{w}} = \tilde{\boldsymbol{w}}_{\mathrm{W}} \tag{11e}$$

The system (11) is a continuous-time, nonlinear system. For a deterministic observer, Eq. (11e) is replaced with $\dot{\boldsymbol{V}}_{\mathrm{w}} = \boldsymbol{0}$ and the term $\boldsymbol{R}_{\mathrm{IB}}^{\mathrm{T}}\tilde{\boldsymbol{w}}_{\mathrm{W}}$ vanishes in Eq. (11c). For nondeterministic observers such as the KF, EKF, and UKF, the terms $\boldsymbol{R}_{\mathrm{IB}}^{\mathrm{T}}\tilde{\boldsymbol{w}}_{\mathrm{W}}$ in Eq. (11c) and $\tilde{\boldsymbol{w}}_{\mathrm{W}}$ in Eq. (11e) will appear as process noise; see Eq. (18). This will be discussed in Sec. VI where model-based wind estimation using a fixed-wing aircraft is implemented using a KF, EKF, and UKF. Estimation algorithms that incorporate a system dynamic model are typically implemented in discrete time. A continuous-time system such as (11) may be discretized by implementing a zero-order hold, for example, on the system inputs. Then, a numerical integration scheme such as Euler or Runge-Kutta integration may be used to obtain model updates. In addition to being implemented in discrete time, many observer structures assume the system dynamics are linear. Equations (11) may be linearized about a given state and input, such as a nominal steady motion or just the most current state and input values, however the domain in which this model is an accurate approximation of (11) will be limited. Following is an overview of the observers algorithm considered here.

B. Deterministic Observer

In cases where measurement noise is absent from a dynamic system, one can construct a Luenberger observer [42] to estimate the states of a discrete-time dynamic system as done in [43–45] for wind estimation. The dynamic model of

a linear time-varying system in the absence of direct throughput and process and measurement noise is

$$\boldsymbol{x}(i) = \boldsymbol{A}(i-1)\boldsymbol{x}(i-1) + \boldsymbol{B}(i-1)\boldsymbol{u}(i-1) \tag{12a}$$

$$\boldsymbol{y}(i-1) = \boldsymbol{C}(i-1)\boldsymbol{x}(i-1) \tag{12b}$$

where $\boldsymbol{x}(i) \in \mathbb{R}^n$ denotes the state vector, $\boldsymbol{u}(i) \in \mathbb{R}^m$ is the vector of inputs, $\boldsymbol{y}(i) \in \mathbb{R}^p$ is the vector of outputs, $\boldsymbol{A}(i) \in \mathbb{R}^{n\times n}$ is the state matrix, $\boldsymbol{B}(i) \in \mathbb{R}^{n\times m}$ is the control input matrix, and $\boldsymbol{C}(i) \in \mathbb{R}^{p\times n}$ is the output matrix. The output model in (12) includes no direct throughput of the input $\boldsymbol{u}(i)$, but one may easily extend the deterministic model to incorporate direct throughput. For the nondeterministic models discussed below, one may include direct throughput with some additional effort as described in [46, §4.4]. The integer $i \in \{1, \ldots, N\}$ denotes the sample index up to some total number of measurements N. For a constant sample time Δt, the time that has elapsed since time $t = 0$ is $(i-1)\Delta t$. In order to estimate the state of this linear system, the pair $(\boldsymbol{A}(i), \boldsymbol{C}(i))$ must be observable. For the pair to be observable on the finite time interval from time step $i = 0$ to $i = N$, the matrix

$$\mathcal{O}(0, N) = \sum_{i=0}^{N} \overline{\boldsymbol{\Phi}}^{\mathrm{T}}(i, 0)\overline{\boldsymbol{C}}^{\mathrm{T}}(i)\boldsymbol{C}(i)\boldsymbol{\Phi}(i, 0)$$

must be positive-definite [47] where $\boldsymbol{\Phi}(i, 0)$ is the discrete-time state transition matrix

$$\boldsymbol{\Phi}(i, 0) = \prod_{j=0}^{i-1} \boldsymbol{A}(j)$$

If the pair $(\boldsymbol{A}(i), \boldsymbol{C}(i))$ is observable, then the measurements can be used to reconstruct the state using the Luenberger observer defined by

$$\hat{\boldsymbol{x}}(i) = \boldsymbol{A}(i-1)\hat{\boldsymbol{x}}(i-1) + \boldsymbol{L}(i-1)(\boldsymbol{y}(i-1) - \hat{\boldsymbol{y}}(i-1)) + \boldsymbol{B}(i-1)\boldsymbol{u}(i-1) \tag{13a}$$

$$\hat{\boldsymbol{y}}(i-1) = \boldsymbol{C}(i-1)\hat{\boldsymbol{x}}(i-1) \tag{13b}$$

where $\hat{\boldsymbol{x}}$ is the state estimate and $\hat{\boldsymbol{y}}$ is the corresponding output. For a well-designed observer, the observer gain $\boldsymbol{L}(i)$ is chosen such that the observer error $\boldsymbol{e}(i) = \hat{\boldsymbol{x}}(i) - \boldsymbol{x}(i)$ converges to zero as i approaches infinity, so that the estimate $\hat{\boldsymbol{x}}(i)$ approaches the true state $\boldsymbol{x}(i)$. The observer error can be rewritten as $\boldsymbol{e}(i) = (\boldsymbol{A}(i-1) - \boldsymbol{L}(i-1)\boldsymbol{C}(i-1))\boldsymbol{e}(i-1)$ using (12) and (13). The origin is a uniformly exponentially stable equilibrium of the observer error equation if and only if a symmetric matrix sequence $\boldsymbol{Q}(i) \in \mathbb{R}^{n\times n}$ exists for all i such that $\eta\mathbb{I} \preceq \boldsymbol{Q}(i) \preceq \rho\mathbb{I}$ and

$$(\boldsymbol{A}(i) - \boldsymbol{L}(i)\boldsymbol{C}(i))^{\mathrm{T}}\boldsymbol{Q}(i+1)(\boldsymbol{A}(i) - \boldsymbol{L}(i)\boldsymbol{C}(i)) - \boldsymbol{Q}(i) \preceq \nu\mathbb{I}$$

for some finite positive constants η, ρ, and ν [48]. The matrix sequences $\boldsymbol{L}(i)$ and $\boldsymbol{Q}(i)$ must be chosen to satisfy the above conditions. Following [48, Thm 29.2], the matrix sequence $\boldsymbol{Q}(i)$ may be chosen as

$$\boldsymbol{Q}(i) = \overline{\boldsymbol{\Phi}}^{\mathrm{T}}(i-l+1, i+1)\mathcal{O}(i-l+1, i+1)\boldsymbol{\Phi}(i-l+1, i+1) \tag{14}$$

for some positive integer l and for all i. Define the following α-weighted variant of the observability Gramian:

$$\mathcal{O}_\alpha(0, N) = \sum_{i=0}^{N} \alpha^{4(l-N+1)}\overline{\boldsymbol{\Phi}}^{\mathrm{T}}(i, 0)\overline{\boldsymbol{C}}^{\mathrm{T}}(i)\boldsymbol{C}(i)\boldsymbol{\Phi}(i, 0)$$

For a constant value $\alpha > 1$, the observer gain

$$\boldsymbol{L}(i) = \left[\overline{\boldsymbol{\Phi}}^{\mathrm{T}}(i-l+1, i+1)\mathcal{O}_\alpha(i-l+1, i+1)\boldsymbol{\Phi}(i-l+1, i+1)\right]^{-1}\boldsymbol{A}^{-\mathrm{T}}(i)\boldsymbol{C}^{\mathrm{T}}(i) \tag{15}$$

ensures uniform exponential stability of the observer error $\boldsymbol{e}(i)$ with rate α. See Chapters 23 and 29 of [48] for more details about stability and state estimation for discrete-time linear, time-varying systems.

Figure 1 shows the Luenberger observer divided into initialization, model-based prediction, and measurement-based correction steps. As stated earlier, $\hat{\boldsymbol{x}}$ and $\hat{\boldsymbol{y}}$ denote the estimated state and output in Figure 1. For the system (12), the state $\boldsymbol{x}$ and output $\boldsymbol{y}$ are deterministic. In the following sections, concerning the KF, EKF, and UKF, the state $\boldsymbol{x}$ and the output $\boldsymbol{y}$ will be subject to random inputs. For these systems, the notation $\hat{\boldsymbol{x}}$ and $\hat{\boldsymbol{y}}$ will indicate conditional probabilities, as defined and discussed in Section IV.C.

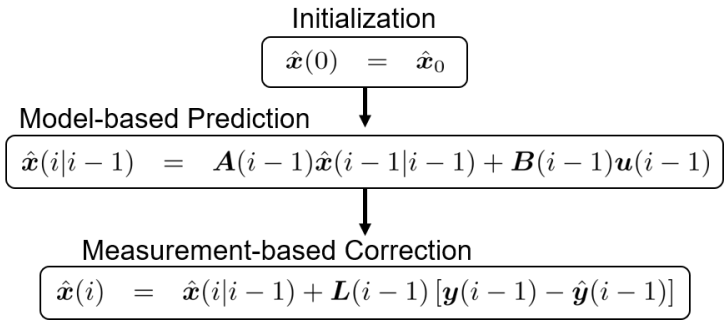

Fig. 1 The Luenberger observer split into initialization, model-based prediction, and measurement-based correction steps where $\hat{\boldsymbol{x}}_0$ is the initial state estimate. See [42], for example.

C. Kalman Filter

The KF is used to estimate the state of a non-deterministic, discrete-time, linear dynamic system. The general form of this system follows, including equations for both the output $\boldsymbol{y}$ and the (noisy) measurement $\boldsymbol{z}$ and omitting direct

throughput from both as discussed earlier:

$$\boldsymbol{x}(i) = \boldsymbol{A}(i-1)\boldsymbol{x}(i-1) + \boldsymbol{B}(i-1)\boldsymbol{u}(i-1) + \boldsymbol{\Gamma}(i-1)\tilde{\boldsymbol{w}}(i-1) \tag{16a}$$

$$\boldsymbol{y}(i) = \boldsymbol{C}(i)\boldsymbol{x}(i) \tag{16b}$$

$$\boldsymbol{z}(i) = \boldsymbol{y}(i) + \tilde{\boldsymbol{v}}(i) \tag{16c}$$

where $\boldsymbol{\Gamma}(i) \in \mathbb{R}^{n\times q}$ is the disturbance input matrix, $\tilde{\boldsymbol{w}}(i) \in \mathbb{R}^q$ is the process noise vector, $\boldsymbol{z}(i) \in \mathbb{R}^p$ is the measurement vector, and $\tilde{\boldsymbol{v}}(i) \in \mathbb{R}^p$ is the vector of measurement noise. For a KF, the measurement and process noise are assumed to be Gaussian, zero mean, white noise sequences [49]. The random forcing $\tilde{\boldsymbol{w}}$ makes the system non-deterministic. When estimating the states of a non-deterministic system, we define the state estimate $\hat{\boldsymbol{x}}$ at a time step i as the expected value of the random variable $\boldsymbol{x}$ at i given the measurement $\boldsymbol{z}$ at $k \leq i$. This conditional probability is denoted

$$\hat{\boldsymbol{x}}(i|k) = E\{\boldsymbol{x}(i)|\boldsymbol{z}(k)\}$$

The state estimate $\hat{\boldsymbol{x}}$ has an associated covariance

$$\boldsymbol{P}(i|k) = E\{[\boldsymbol{x}(i) - \hat{\boldsymbol{x}}(i|k)][\boldsymbol{x}(i) - \hat{\boldsymbol{x}}(i|k)]\mathrm{T}|\boldsymbol{z}(k)\}$$

for $k \leq i$. The steps of Kalman filtering, as described in [49], are shown in Figure 2. The steps are grouped into three categories: initialization, prediction, and correction. The matrix $\boldsymbol{P}_0$ is the covariance of the initial state estimate $\hat{\boldsymbol{x}}(0|0)$. The covariance matrix sequences $\boldsymbol{Q}(i)$ and $\boldsymbol{R}(i)$ of the zero-mean, white, Gaussian process and measurement noise, respectively, are assumed to be known.

KF-based wind estimation is used in [19, 50–53]. These estimation schemes assume the UAV is operating about some nominal trajectory, such as wings-level, constant-altitude flight for fixed-wing UAVs or hovering flight for multirotors. An example of KF-based wind estimation using a fixed-wing UAV is provided in Section VI.

D. Extended Kalman Filter

The EKF is an adaptation of the KF's linear minimum mean square error estimation algorithm to nonlinear systems. In the EKF, nonlinear terms in the state and output equations are linearized at each time step about the current state

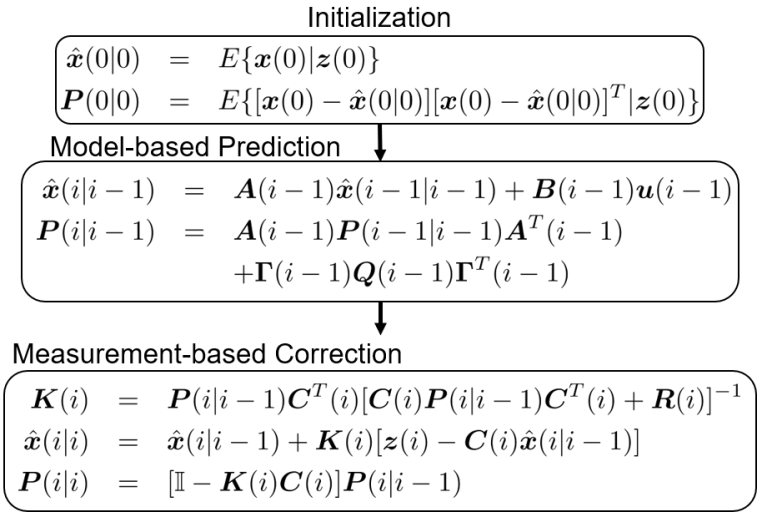

Fig. 2 KF algorithm based on the linear system (16) split into three steps, where $\mathbb{I}$ is the $n \times n$ identity matrix. See [49], for example.

estimate and input. Consider the discrete-time nonlinear dynamic system

$$\boldsymbol{x}(i) = \boldsymbol{f}\Big(\boldsymbol{x}(i-1), \boldsymbol{u}(i-1), \tilde{\boldsymbol{w}}(i-1)\Big) \tag{17a}$$

$$\boldsymbol{y}(i) = \boldsymbol{h}\Big(\boldsymbol{x}(i)\Big) \tag{17b}$$

$$\boldsymbol{z}(i) = \boldsymbol{y}(i) + \tilde{\boldsymbol{v}}(i) \tag{17c}$$

where the vector fields $\boldsymbol{f}$ and $\boldsymbol{h}$ are assumed to contain once continuously differentiable nonlinear functions of the states, process noise, and inputs. The measurement and process noise are assumed to be Gaussian, zero mean, white noise sequences. Figure 3 shows the steps of EKF implementation for the system (17).

Wind estimation using an EKF is described in [54–60]. Since the EKF requires linearization at each time step, it can be computationally expensive and difficult to implement in real-time wind field estimation. However, the EKF relaxes the requirement that the system state remain within a small neighborhood of a nominal state provided the local linearization approximates the nonlinear dynamics with sufficient accuracy during each sample interval.

E. Unscented Kalman Filter

The unscented Kalman filter (UKF) provides another approach to nonlinear estimation for non-deterministic systems. First described by Julier and Uhlmann in [61], the UKF is based on the unscented transformation which is a method for approximating a random variable that undergoes a nonlinear transformation. The UKF does not require the computation of Jacobian matrices, which can make its implementation simpler [62]. For the system (17), the state vector $\boldsymbol{x}$ is a random variable, with expected value $\hat{\boldsymbol{x}}$ and covariance $\boldsymbol{P}_{xx}$, which is propagated through the nonlinear functions $\boldsymbol{f}$

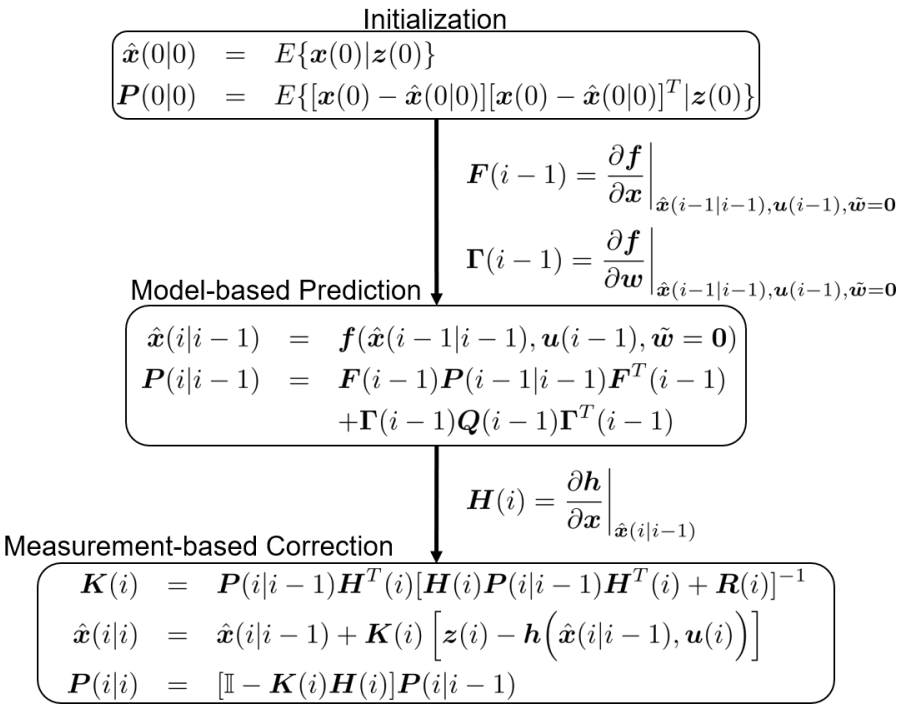

Fig. 3 EKF algorithm based on the nonlinear system (17) split into three steps with recursive linearization. See [49], for example.

and $\boldsymbol{h}$. The unscented transformation involves selecting n-dimensional vectors, called sigma points, around $\hat{\boldsymbol{x}}$ and then computing weights associated with each sigma point based on the statistics of $\boldsymbol{x}$. For the system (17), the $2(n+q)+1$ sigma points are [63]:

$$
\begin{aligned}
&\boldsymbol{\chi}_0 = \hat{\boldsymbol{x}} && \\
&\boldsymbol{\chi}_j = \hat{\boldsymbol{x}} + \sqrt{(n+p+q+\lambda)\boldsymbol{P}_{xx}}, && j = 1, \ldots, n \\
&\boldsymbol{\chi}_j = \hat{\boldsymbol{x}} - \sqrt{(n+p+q+\lambda)\boldsymbol{P}_{xx}}, && j = n+1, \ldots, 2n \\
&\boldsymbol{\chi}_j = \hat{\boldsymbol{x}} && j = 2n+1, \ldots, 2n+2q \\
&\boldsymbol{\chi}_j^w = \boldsymbol{0}, && j = 0, \ldots, 2n \\
&\boldsymbol{\chi}_j^w = \sqrt{(n+p+q+\lambda)\boldsymbol{Q}}, && j = 2n+1, \ldots, 2n+q \\
&\boldsymbol{\chi}_j^w = -\sqrt{(n+p+q+\lambda)\boldsymbol{Q}}, && j = 2n+q+1, \ldots, 2n+2q
\end{aligned}
$$

where $\lambda = \alpha^2(n+q+\kappa) - (n+q)$ is a sigma point scaling parameter. The scaling parameter λ depends on two other parameters, α and κ, where α is a small, positive value reflecting the spread of the sigma points (typically, $10^{-4} < \alpha < 1$) and κ is a secondary scaling parameter tuned to reduce prediction error [61]. For a Gaussian distribution, it is recommended to set $\kappa = 0$ [63].

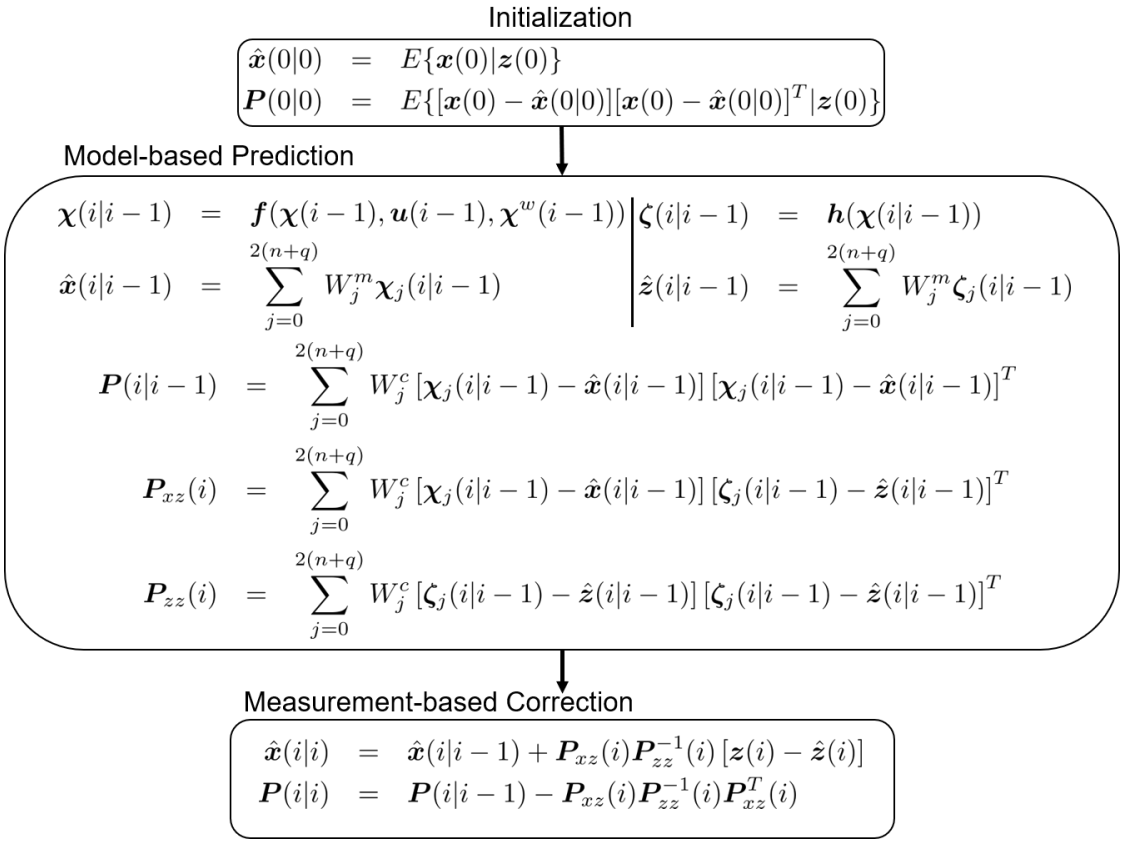

Fig. 4 UKF algorithm based on the nonlinear system (17) split into three steps using computed sigma points and weights. See [63], for example.

The general steps of the UKF including initialization, prediction, and correction are provided in Figure 4, where each of the weights W_j^m and W_j^c for each vector of sigma points are

$$\begin{aligned} W_0^m &= \frac{\lambda}{n+q+\lambda} \\ W_0^c &= \frac{\lambda}{n+q+\lambda} + 1 - \alpha^2 + \beta \\ W_j^m &= W_j^c = \frac{1}{2(\lambda+n+q)} \end{aligned}$$

for $j = 1, \ldots, 2n + 2q$ and where β is used to incorporate knowledge of the distribution of $\boldsymbol{x}$. The authors of [63] note, for example, that a Gaussian distribution is best represented by $\beta = 2$. Compared to the EKF algorithm, the UKF algorithm requires the additional step of computing sigma points and weights; the computational cost is about twice that of an EKF. As noted earlier, though, the approach does not require the computation of Jacobian matrices and the UKF exhibits other performance and accuracy advantages. Examples of wind estimation using a UKF can be found in [62, 64–68].

V. Summary of Existing Work on Wind Estimation

As discussed in Section I, wind field estimation using UAVs can be accomplished by measuring the relative wind velocity directly or by inferring the wind velocity from the aircraft motion. Wind estimates obtained using indirect methods, the focus of this survey, are validated by comparing the obtained estimates with a truth source, such as a direct measurement obtained using a dedicated sensor installed on the aircraft [69]. Given the measurements or estimates of the inertial velocity and the air-relative velocity, the wind velocity can be obtained from the wind triangle relationship in Figure 5, as expressed in Eqn. (7a).

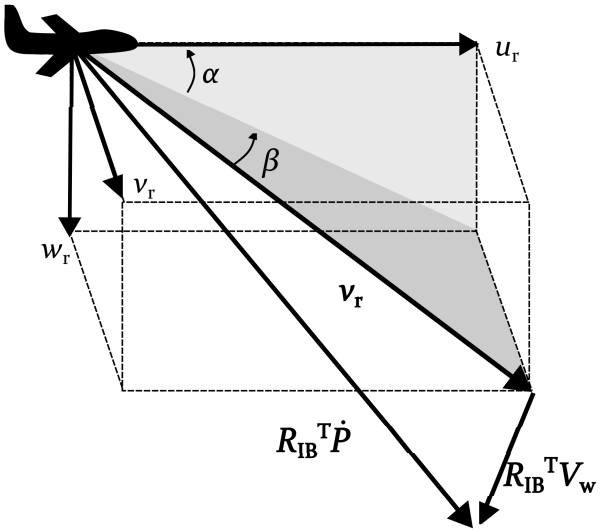

Fig. 5 Illustration of the wind triangle including AoA and AoS.

The wind field can be separated into steady and turbulent wind components, as discussed in Section II.B. Turbulence models can be incorporated into wind estimation algorithms. They are also used to construct realistic wind simulations as truth models to evaluate the quality of wind estimates obtained using different algorithms. When considering turbulent wind field effects on aircraft motion, the Dryden and von Kármán turbulence models for clear air turbulence are commonly used [24]. Turbulence models can be incorporated into indirect wind estimation schemes, such as in [66] and [70] where wind is incorporated using the Dryden turbulence model. Other turbulence models exist, such as the Kaimal [71] and Mann [72] turbulence models, but to the authors' knowledge they have not been employed for wind estimation using UAVs. Turbulent wind can also be modeled as a simple Gauss-Markov sequence as in [73].

Indirect wind estimation methods using UAVs to solve the wind triangle relationship can be categorized as model-based and model-free. Model-based methods use the aircraft's kinematic and dynamic equations to estimate components of the wind vector whereas model-free methods do not require knowledge of the aircraft's dynamic model. These methods are coupled with different types of estimators to compute components of the wind vector and they require

measurements from various operational sensors onboard a UAV. The UAVs used for wind estimation are typically equipped with a GNSS receiver that provides position and velocity with respect to the NED frame, an IMU that provides the aircraft's specific acceleration and angular velocity, a magnetometer that provides heading, and a Pitot probe to measure airspeed. Additionally, aircraft may be instrumented with flow vanes or multihole Pitot probes to obtain angle of attack (AoA) and angle of sideslip (AoS) measurements. A sensor that provides airspeed, AoA, and AoS is referred to as an air data sensor (ADS).

Existing work on wind estimation formulations and different estimation techniques is summarized in Table 1. Table 1 also includes work where model-based and model-free methods are combined for wind estimation. Combined methods seek to use some knowledge of an aircraft's aerodynamic model and to alleviate some restrictions from model-free estimation methods such as the requirement for persistently exciting aircraft motions to resolve 3D air relative velocity when 3D measurements are not available.

A. Model-based Methods

Model-based wind estimation methods rely on knowledge of the aircraft flight dynamic model. Developing this model can involve ground testing to determine inertial properties, wind tunnel testing to determine propulsion models [64], and experimental and computational model identification to determine the aerodynamic force and moment structure and parameters [44, 74, 75]. Model-based wind estimation schemes can be applied to deterministic or non-deterministic systems which use linear or nonlinear dynamic models. Other methods of wind estimation include optimization techniques, which rely on solving nonlinear optimal control problems, and include multi-objective optimization and model predictive static programming (MPSP) [76, 77].

References [9, 78–80] introduce tilt-based methods (denoted "Tilt" in Table 1) for wind estimation using multirotor aircraft. The tilt-based wind estimation scheme is based on the deviation of the multirotor attitude from a trim hover condition. It is assumed that the deviation is a result of a wind disturbance. This method requires only attitude and position data from the GNSS and IMU sensors onboard the multirotor aircraft. Palomaki *et al.* compare direct wind measurements using a sonic anemometer mounted on a hexacopter to indirect model-based estimation using attitude data from a quadcopter using only hovering flight [78]. Segales *et al.* fly the CopterSonde, a multirotor aircraft developed for remote sensing in the atmospheric boundary layer, to obtain experimental 2D estimates of the wind based on tilt measurements [9]. The wind velocity is calculated using pitch angle measurements by programming the CopterSonde to hover in "wind vane" mode where it orients itself to face the wind, keeping its roll angle near zero. Neumann *et al.* identify a quadcopter aerodynamic model with wind tunnel testing and perform tilt-based real-time wind estimation [79]. They solve the wind triangle relationship for the wind velocity using GNSS-based inertial velocity measurements and estimate air-relative velocity using the identified aerodynamic model with IMU and magnetometer measurements. Shelekhov *et al.* estimate atmospheric turbulence using three commercial off-the-shelf multirotor aircraft in hover at

different vertically spaced points [80]. The time histories and spectral content of the quadcopter wind estimation results are compared with measurements from three anemometers placed at different altitudes.

In [43–45] the wind is modeled as a deterministic process and the linearized equations of motion of the system are used to obtain wind estimates using a deterministic observer. González-Rocha *et al.* [43] present three quadrotor models: a kinematic particle model, a dynamic particle model, and a rigid body model. They obtain 2D wind velocity estimates using the two particle models by directly solving the wind triangle relationship for wind velocity using measurements of inertial and air-relative velocity from GNSS, IMU, magnetometer, and barometer data. In [44], the authors compare wind velocity estimates obtained using the three quadcopter models to measurements from a sonic anemometer. The rigid body model given by the system (10) is linearized about steady straight and level forward flight and the state is augmented to include the wind velocity, assuming the wind to be slowly varying compared to the aircraft motion. It was found that increasing the fidelity of the model resulted in more accurate wind speed estimates, with the rigid body model providing the best wind speed estimates. In [45] the rigid body model is used to estimate wind velocity with a quadcopter in hover and in steady ascent where the quadcopter aerodynamic force and moment models were identified using stepwise regression and output error parameter estimation using flight test data. This study also assumed the wind to be slowly varying compared to the aircraft and compared wind velocity estimates in hover and steady ascent to wind velocities measured using sound detecting and ranging (SoDAR). The dynamic particle model of a multirotor is also used in [51] where wind estimation assuming a slowly varying wind field relative to the aircraft is presented using a KF along with a parameter identification method to estimate the drag model of the aircraft. Xiang *et al.* present quadcopter-based wind estimation using a KF where estimates were obtained experimentally with the quadcopter in steady flight in a straight line and in a steady hover [52]. The estimates obtained in hover were in closer agreement with measurements obtained using digital anemometers attached to masts in the test environment.

Model-based wind estimation methods using either KFs or EKFs are applied in [19, 51–53, 55, 57–59, 75, 81]. Both types of filter rely on linearizing the nonlinear system equations. For the KF, the nonlinear equations of motion are linearized about a nominal state. For the EKF, the nonlinear system is linearized about the current state estimate at each time step. Torgesen *et al.* estimate steady and turbulent air wake stream components using an error-state Kalman filter for a hexacopter tethered behind a cruising vessel [12]. Langelaan *et al.* [19] assume a polynomial structure for the wind to simplify the parameter estimation method which allows implementation of a KF for state estimation. In [19], the motivation for obtaining wind estimates is to be able to query the wind field in real-time to facilitate autonomous dynamic soaring. Petrich *et al.* use a two-state KF that initially generates a GNSS-based position estimate and then estimates orientation, airspeed, angular rate, and 3D wind velocity based on measurements from an IMU and an air data sensor under the assumption of a constant wind field [53]. Chen *et al.* design an invariant-EKF (IEKF) that leverages the invariant dynamics of quadcopter kinematics and translational dynamics to obtain estimates with errors that are realistic with respect to the symmetries exhibited by the system [55]. Lie *et al.* present a wind estimation method

that relies only on GNSS and inertial navigation system (INS) measurements using a cascaded EKF structure under the assumption of small AoA and constant thrust [57]. In [58], Sun *et al.* propose wind estimation, where the wind is modeled as a random walk process, using a tail-sitter UAV that is able to operate in three flight regimes: rotary, transitional, and wing-borne flight. They use the cascaded EKF structure from [57]. Tian *et al.* propose an estimation method modeling the wind as a random walk process using two EKFs where the first EKF estimates AoA and AoS and the second estimates air-relative velocity, orientation, and wind velocity using measurements from GNSS, IMU, and a Pitot probe [59]. In [75], Halefom *et al.* investigate the benefits of including unsteady aerodynamics in a model-based wind estimator for a small, fixed-wing aircraft, and present the outcomes of an experimental implementation. The study involves the design of an extended Kalman filter for two motion models derived from flight data, one accounting for unsteady effects and another that does not. The resulting wind estimates are then compared with the local wind velocity reconstructed from measurements obtained from an air data sensor equipped with wind vanes and a Kiel probe. Pappu *et al.* use an EKF to estimate wind gusts with a quadcopter in hover using only GNSS, IMU, and control actuation sensors assuming that gusts can be represented by filtered white noise [81].

The UKF is used for model-based wind estimation in [62, 64–66, 68, 82]. The UKF does not require analytical linearization of the nonlinear equations of motion about a nominal state. Condomines *et al.* present wind estimation and aircraft parameter identification based on flight experiments using a fixed-wing UAV where a square root UKF-based approach is proposed for simultaneous aircraft air-relative velocity and wind velocity estimation assuming the spatial gradient of the wind field to be zero [64]. Larrabee *et al.* investigate the use of a stand-alone UKF and a cooperative UKF for a leader-follower formation of fixed-wing aircraft where the follower senses the wake of the leader [65]. Rhudy *et al.* estimate wind velocity and acceleration components assuming the wind acceleration is a random walk process using a UKF in [62] and in [68] UKF-based wind estimates are compared under two different models for the random wind variations: (1) a random walk and (2) a Gauss-Markov process. Lee *et al.* use a square-root UKF for wind and aircraft state estimation where the aircraft is exposed to time-varying prevailing wind and turbulence modeled using the Dryden turbulence model and both the wind velocity and its derivative are estimated [66]. Cooper *et al.* perform quadcopter wind estimation with a UKF where the motivation is to use wind estimates in a source localization algorithm in two scenarios: (1) a hovering quadcopter and (2) a quadcopter that hovers for 10 seconds then moves to a sequence of two waypoints, loitering at each for 10 seconds [82]. In this work, a flight dynamic model is identified which incorporates rotor blade flapping motion using blade element theory.

Optimization techniques such as model predictive static programming (MPSP) and multi-objective optimization are also employed in model-based wind estimation in [76, 77] and [83], respectively. Hong *et al.* use tracking MPSP (T-MPSP) in [76] and generalized MPSP (G-MPSP) in [77] to estimate 3D wind without requiring any airspeed measurements. In [76], the wind vector is estimated by considering it to be an input to the aircraft model that results in reduced error between the aircraft's measured and predicted kinematic states. The G-MPSP approach in [77] considers

the wind as a virtual input to the model and uses measurements from a previous finite horizon of 0.2 seconds to reduce terminal errors using the measured and predicted states. In [83], Velasco-Carrau *et al.* use multi-objective optimization (MO) for wind estimation and aircraft model identification where an aircraft model structure is provided and MO provides wind speed estimates that are used in model structure determination to correct airspeed-dependent terms and minimize the defined cost functions.

Other model-based wind estimation methods include frequency-based wind gust estimation using a nonlinear disturbance observer [84], wind gust estimation with a quadrotor in a quasi-hover using an unknown input observer (UIO) [85], direct computation of the wind velocities [86], wind velocity estimation using Gaussian process regression (GPR) [87], estimating time-varying wind parameters from quadrotor data using finite time estimation (FTE) [88], wind velocity and aircraft aerodynamic coefficient estimation using a moving horizon estimator (MHE) [70], and ambient wind estimation using an active particle filter (APF) from radio-controlled (RC) helicopter data [11].

B. Model-free Methods

Wind estimation methods that do not require a flight dynamic model are referred to as model-free methods. Model-free methods typically rely on airspeed measurements from a Pitot probe and inertial velocity from GNSS. These methods are attractive because they do not require a lengthy model identification effort. However, model-free estimation methods typically require persistent excitation of the aircraft motion to resolve the air-relative velocity from the scalar airspeed measurement provided by the Pitot probe. Model-free wind estimation with UAVs is used in [50, 56, 60, 89, 90].

The combination of operational sensors available on an aircraft guides the selection of a wind estimation approach. The different combinations of operational sensor suites and wind estimation methods described in the literature reviewed here are shown in Table 2. Model-free wind estimation methods typically rely only on GNSS and Pitot probe data, as described in [50] and [56]. Balmer *et al.* adopt a KF to obtain wind estimates [50]. They assume a constant wind field and provide their algorithm with pseudo-measurements of AoA and AoS to calculate the air-relative velocity. These pseudo-measurements are the equilibrium values of AoA and AoS for the aircraft, assuming that pitch and yaw stability ensures only small deviations from these equilibrium values. This approach allows the authors to remove the requirement for persistent excitation or attitude variations typically seen in model-free wind estimation. Cho *et al.* describe model-free wind estimation where the aircraft is equipped with a single GNSS antenna/receiver and a Pitot probe [56]. They assume a constant 2D wind field and enforce persistent excitation of the aircraft motion, in the form of banking turns and circling maneuvers, to resolve the air-relative velocity and the wind velocity using an EKF.

In addition to GNSS and Pitot probe measurements, instrumentation for model-free wind estimation can include IMU, magnetometer, and/or ADS data. Reference [89] describes wind estimation from data obtained using a fixed-wing UAV equipped with a multihole Pitot probe, an IMU, and a GNSS receiver. The authors compare the accuracy of estimates obtained when incorporating the air-relative velocity measurements in the filter with the accuracy of estimates

obtained when omitting flow sensor data and using persistent excitation. Zhang *et al.* require GNSS, IMU, Pitot probe, and barometric pressure measurements for online calibration of a Pitot probe and wind field estimation with a quadcopter in hovering flight [60]. Witte *et al.* use GNSS, IMU, magnetometer, and a multihole Pitot probe data from a fixed-wing UAV to obtain wind velocity estimates where the GNSS measurements provide inertial velocity and the multihole Pitot probe provides the three components of air-relative velocity. These measurements, along with an attitude estimate from the IMU and magnetometer, allow one to solve the wind triangle for the wind velocity [90]. In [67], Rhudy *et al.* present four different formulations for wind estimation using a UKF with two model-free methods, one of which is based on the work in [56], and two model-based methods. They use GNSS, IMU, and ADS measurements in their estimation algorithms.

C. Combined Methods

In the literature reviewed here, the combined wind estimation methods used either EKFs [54], deterministic observers [91], or moving horizon estimators [17, 70]. Wenz *et al.* use an EKF with GNSS, IMU, and Pitot probe measurements to obtain steady wind and turbulent fluctuation estimates [54]. Attitude changes are required during the flight to maintain observability. Borup *et al.* implement a nonlinear observer for model-free wind estimation, eliminating the persistent excitation requirement by incorporating a simple aerodynamic model that is updated using propeller speed and Pitot probe measurements [91]. The authors note that the simple, assumed aerodynamic model introduces errors into the estimates. Benders *et al.* use a moving horizon estimator and combine wind velocity-based path planning with wind velocity estimation where wind is modeled using the Dryden turbulence model [17]. This method requires aircraft attitude changes during the flight to maintain observability. It is considered a combined method as the aerodynamic coefficients of the aircraft are determined online rather than beforehand. Wenz *et al.* [70] model the wind using the Dryden turbulence model and obtain wind velocity and turbulence estimates using a moving horizon estimator where persistent excitation is required to distinguish between changes in aerodynamic coefficients and the wind velocity.

VI. Implementation

In this section, we demonstrate the implementation of a wind estimation scheme using the KF, EKF, and UKF. These filters are widely used estimation tools which play a role in many of the papers discussed here. Although some authors report better results using alternative algorithms, the KF, EKF, and UKF serve as useful illustrations of the general estimation process. For tutorial purposes, we have implemented model-based, indirect wind estimation using a fixed-wing UAV for which a motion model has been identified from flight test data. The aircraft is equipped with an IMU, GPS receiver, and pitot-static probe that provide the measurements required to estimate the extended state (i.e., the state of aircraft motion and the wind velocity). Using the flight dynamic model, we obtain simulated flight data for which the aircraft experiences input perturbations and wind disturbances. We then implement various filters to obtain

Table 1 Summary of reviewed indirect wind estimation formulation and filtering methods using small UAVs. The symbols denote the type of aircraft used: ✈ = fixed-wing, ✕ = multirotor, and ✈✕ = lift+cruise. The symbol † indicates wind estimation approaches that were validated using experimental flight test data.

Model-based	Model-free	Combined
	Kalman Filter	
Hattenberger *et al.*† [51] ✕		
Langelaan *et al.*† [19] ✈	Balmer *et al.*† [50] ✈	
Xiang *et al.*†[52] ✕		
Petrich *et al.*† [53] ✈		
	Extended Kalman Filter	
Chen *et al.* [55] (IEKF) ✕		
Lie *et al.*† [57] ✈		
Pappu *et al.*† [81] ✕	Cho *et al.*† [56] ✈	
Sun *et al.* † [58] ✈	Rautenberg *et al.*† [89] ✈	Wenz *et al.* [54] ✈
Tian *et al.*† [59] ✈	Zhang *et al.*† [60] ✈✕	
Torgesen *et al.*† [12] ✕		
Halefom *et al.*† [75] ✈		
	Unscented Kalman Filter	
Condomines *et al.*† [64] ✈		
Cooper *et al.* [82] ✕		
Larrabee *et al.*† [65] ✈	Rhudy *et al.*† [67] ✈	
Lee *et al.* [66] ✈		
Rhudy *et al.*† [62, 67, 68] ✈		
	Deterministic Observer	
Asignacion *et al.*† [84] ✕		Borup *et al.* [91] ✈
Gonzalez-Rocha *et al.*† [43–45] ✕		
	Other	
Azid *et al.*† [85] (UIO) ✕		
Hong *et al.* [76] (T-MPSP) ✈		
Kumar *et al.*† [11] (APF) ✕		
Langelaan *et al.* [86] ✈		
Marinescu *et al.*† [87] (GPR) ✈		
Meier *et al.*† [92]✕		
Neumann *et al.*† [79] (Tilt) ✕	Witte *et al.*† [90] ✈	Benders *et al.* [17](MHE) ✈
Palomaki *et al.*† [78] (Tilt) ✕		Wenz *et al.*† [70](MHE) ✈
Perozzi *et al.* [88] (FTE)		
Salazar *et al.*† [93] ✈		
Segales *et al.*† [9] (Tilt) ✕		
Shelekhov *et al.*† [80] (Tilt) ✕		
Velasco *et al.*† [83] ✈		
Wenz *et al.*† [70] (MHE) ✈		

Table 2 Indirect wind estimation formulations by operational sensor suite, where * indicates reference also uses linear optical sensor arrays, ** indicates reference also uses control inputs, * indicates reference also uses a range sensor, † indicates reference uses a barometer and vision-based prose, and ‡ indicates reference also uses a multihole Pitot probe.**

Model-based	Model-free	Combined
IMU		
Segales *et al.* [9]		
IMU and magnetometer		
Palomaki *et al.* [78]		
GNSS and Pitot probe		
Hattenberger *et al.* [51]	Balmer *et al.* [50]	
Hong *et al.* [76]	Cho *et al.* [56]	
GNSS and IMU		
Cooper *et al.*** [82], Pappu *et al.*** [81]		
Phelps *et al.* [13], Salazar *et al.* [93]		
Sun *et al.* [58], Tian *et al.* [59]		
Torgesen *et al.*† [12], Velasco-Carrau *et al.*** [83]		
Xiang *et al.*[52]		
GNSS, IMU, and magnetometer		
Chen *et al.* [55], Perozzi *et al.* [88]		
Kumar *et al.** [11]		
GNSS, IMU, barometer, and magnetometer		
Gonzelez-Rocha *et al.* [43–45], Neumann *et al.* [79]		
Shelekhov *et al.* [80], Halefom *et al.* [75]		
GNSS, IMU, and Pitot probe		
Condomines *et al.* [64]	Rautenberg *et al.* [89]	Benders *et al.* [17]
Lie *et al.* [57]		Borup *et al.* [91]
		Wenz *et al.* [54, 70]
GNSS, IMU, Pitot probe, and magnetometer		
Azid *et al.* [85], Langelaan *et al.* [19, 86]	Witte *et al.*‡ [90]	
Marinescu *et al.* [87], Meier *et al.* [92]	Zhang *et al.* [60] (w/ barometer)	
GNSS, IMU, and ADU		
Larrabee *et al.* [65]***, Petrich *et al.* [53]	Rhudy *et al.* [67]	
Rhudy *et al.* [62, 67, 68]		
GNSS, IMU, ADU, and magnetometer		
Lee *et al.* [66]		

estimates of the wind velocity. Specifically, we compare wind velocity estimates obtained using either a KF, EKF, or UKF. The wind field is generated using the two-dimensional von Kármán turbulence model. The simulated data serve as truth data for comparing the filter results.

A. Augmented Dynamic Model of the Aircraft for Wind Estimation

To illustrate indirect, model-based wind estimation, we start by considering the dynamics of a fixed-wing aircraft in wind. The wind velocity $\boldsymbol{V}_{\mathrm{W}}$ is appended to the aircraft state in the 15×1 augmented state vector $\boldsymbol{x} = [\boldsymbol{P}, \boldsymbol{\Theta}, \boldsymbol{v}_{\mathrm{r}}, \boldsymbol{\omega}, \boldsymbol{V}_{\mathrm{w}}]\,\mathrm{T}$. The equations of motion of the augmented system are

$$\dot{\boldsymbol{P}} = \boldsymbol{R}_{\mathrm{IB}}\boldsymbol{v}_{\mathbf{r}} + \boldsymbol{V}_{\mathrm{w}} + \tilde{\boldsymbol{w}}_P \tag{18a}$$

$$\dot{\boldsymbol{\Theta}} = \boldsymbol{L}_{\mathrm{IB}}\boldsymbol{\omega} + \tilde{\boldsymbol{w}}_\Theta \tag{18b}$$

$$\dot{\boldsymbol{v}}_{\mathrm{r}} = \boldsymbol{v}_{\mathrm{r}} \times \boldsymbol{\omega} + \frac{1}{m}\boldsymbol{F}_A(\boldsymbol{v}_{\mathrm{r}}, \boldsymbol{\omega}, \boldsymbol{\delta}) + \frac{1}{m}\boldsymbol{R}_{\mathrm{IB}}^{\mathrm{T}}\boldsymbol{F}_G + \tilde{\boldsymbol{w}}_{v_{\mathrm{r}}} \tag{18c}$$

$$\dot{\boldsymbol{\omega}} = \boldsymbol{I}^{-1}\left(\boldsymbol{I}\boldsymbol{\omega} \times \boldsymbol{\omega}\right) + \boldsymbol{I}^{-1}\boldsymbol{M}_A(\boldsymbol{v}_{\mathrm{r}}, \boldsymbol{\omega}, \boldsymbol{\delta}) + \tilde{\boldsymbol{w}}_\omega \tag{18d}$$

$$\dot{\boldsymbol{V}}_{\mathrm{w}} = \tilde{\boldsymbol{w}}_{\mathrm{W}} \tag{18e}$$

where the 4×1 input vector $\boldsymbol{\delta} = [\delta_{\mathrm{e}}, \delta_{\mathrm{a}}, \delta_{\mathrm{r}}, \delta_{\mathrm{rps}}]$ comprises the conventional elevator, aileron, rudder, and thrust commands. The vector $\tilde{\boldsymbol{w}} = [\tilde{\boldsymbol{w}}_P, \tilde{\boldsymbol{w}}_\Theta, \tilde{\boldsymbol{w}}_{v_{\mathrm{r}}}, \tilde{\boldsymbol{w}}_\omega, \tilde{\boldsymbol{w}}_{\mathrm{W}}]\mathrm{T}$ represents the process noise. The 3×1 vectors $\tilde{\boldsymbol{w}}_P$ and $\tilde{\boldsymbol{w}}_\Theta$ are process noise signals that account for error due to the linearization of Eqs. (18a) and (18b). Similarly, the 3×1 process noise vectors $\tilde{\boldsymbol{w}}_{v_{\mathrm{r}}}$ and $\tilde{\boldsymbol{w}}_\omega$ account for the error due to the linearization of Eqs. (18c) and (18d) as well as aerodynamic modeling error in $\boldsymbol{F}_A$ and $\boldsymbol{M}_A$. Additionally, $\tilde{\boldsymbol{w}}_{v_{\mathrm{r}}}$ accounts for the term $\boldsymbol{R}_{\mathrm{IB}}^{\mathrm{T}}\tilde{\boldsymbol{w}}_{\mathrm{W}}$ in Eq. (11c), where, $\tilde{\boldsymbol{w}}_{\mathrm{W}}$ is a 3×1 vector described in Section II.B. The vectors $\boldsymbol{F}_A$ and $\boldsymbol{M}_A$ are the aerodynamic force and moment, which are modeled using dimensionless coefficients as follows:

$$\boldsymbol{F}_A = \frac{1}{2}\rho||\boldsymbol{v}_{\mathrm{r}}||^2 S \begin{pmatrix} C_X(\boldsymbol{v}_{\mathrm{r}}, \boldsymbol{\omega}, \boldsymbol{\delta}) \\ C_Y(\boldsymbol{v}_{\mathrm{r}}, \boldsymbol{\omega}, \boldsymbol{\delta}) \\ C_Z(\boldsymbol{v}_{\mathrm{r}}, \boldsymbol{\omega}, \boldsymbol{\delta}) \end{pmatrix} + D^4\rho\eta_e\eta_n\delta_{\mathrm{rps}}^2 \begin{pmatrix} C_J(\boldsymbol{\delta}) \\ 0 \\ 0 \end{pmatrix} \qquad \boldsymbol{M}_A = \frac{1}{2}\rho||\boldsymbol{v}_{\mathrm{r}}||^2 S \begin{pmatrix} bC_l(\boldsymbol{v}_{\mathrm{r}}, \boldsymbol{\omega}, \boldsymbol{\delta}) \\ \bar{c}C_m(\boldsymbol{v}_{\mathrm{r}}, \boldsymbol{\omega}, \boldsymbol{\delta}) \\ bC_n(\boldsymbol{v}_{\mathrm{r}}, \boldsymbol{\omega}, \boldsymbol{\delta}) \end{pmatrix}$$

where $\bar{c}$ is the mean aerodynamic chord, b is the wingspan, S is the aircraft wing surface area, ρ is the air density, η_e is the efficiency constant of the aircraft's propellers, η_n is the number of propellers of the aircraft, and D is the diameter of the aircraft's propellers. The non-dimensional thrust, aerodynamic force, and aerodynamic moment vectors are given by $[C_J, 0, 0]$ T, $[C_X, C_Y, C_Z]$ T and $[C_l, C_m, C_n]$ T which depend on air-relative velocity, air-relative angular velocity, and the control inputs. The non-dimensional aerodynamic force and moment models for the aircraft considered in this paper

are

$$C_J = C_{J_0} + C_J J + C_{J^2} J^2 \tag{19a}$$

$$C_X = C_{X_0} + C_{X_{\delta_e}} \delta_e + C_{X_\alpha} \alpha \tag{19b}$$

$$C_Z = C_{Z_0} + C_{Z_q} \hat{q} + C_{Z_\alpha} \alpha \tag{19c}$$

$$C_m = C_{m_0} + C_{m_q} \hat{q} + C_{m_{\delta_e}} \delta_e + C_{m_\alpha} \alpha \tag{19d}$$

$$C_Y = C_{Y_p} \hat{p} + C_{Y_\mathrm{r}} \hat{r} + C_{Y_{\delta_a}} \delta_a + C_{Y_{\delta_\mathrm{r}}} \delta_\mathrm{r} + C_{Y_\beta} \beta \tag{19e}$$

$$C_l = C_{l_p} \hat{p} + C_{l_{\delta_a}} \delta_a + C_{l_\beta} \beta \tag{19f}$$

$$C_n = C_{n_\mathrm{r}} \hat{r} + C_{n_{\delta_a}} \delta_a + C_{n_{\delta_\mathrm{r}}} \delta_\mathrm{r} + C_{n_\beta} \beta \tag{19g}$$

where the nondimensional terms in Eq. (19) are

$$\alpha = \tan^{-1}\left(\frac{w_\mathrm{r}}{u_\mathrm{r}}\right) \quad \beta = \sin^{-1}\left(\frac{v_\mathrm{r}}{||\boldsymbol{v}_\mathbf{r}||}\right) \quad \hat{p} = \frac{pb}{2||\boldsymbol{v}_\mathrm{r}||} \quad \hat{q} = \frac{q\bar{c}}{2||\boldsymbol{v}_\mathrm{r}||} \quad \hat{r} = \frac{rb}{2||\boldsymbol{v}_\mathrm{r}||} \quad J = \frac{||\boldsymbol{v}_\mathrm{r}||}{\delta_\mathrm{rps} D}$$

Numerical values for the coefficients are determined for the particular aircraft considered here through experimental model identification [*].

B. Measurement Model for Wind Estimation

As described in Section IV, the implementation of the KF, EKF, and UKF includes a measurement model. Here, we assume that the aircraft's inertial position and attitude are measured along with the translational and angular velocity with respect to inertial space, expressed in the body reference frame. The 12×1 measurement vector $\boldsymbol{z} = \boldsymbol{y}(\boldsymbol{x}) + \tilde{\boldsymbol{\nu}}$ and the augmented state $\boldsymbol{x} = [\boldsymbol{P}, \boldsymbol{\Theta}, \boldsymbol{v}_\mathrm{r}, \boldsymbol{\omega}, \boldsymbol{V}_\mathrm{W}]\,\mathrm{T}$ have a nonlinear relationship, where the measurement model $\boldsymbol{y}(\boldsymbol{x})$ is

$$\boldsymbol{y} = \begin{pmatrix} \mathrm{I}_3 & \mathbf{0}_3 & \mathbf{0}_3 & \mathbf{0}_3 & \mathbf{0}_3 \\ \mathbf{0}_3 & \mathrm{I}_3 & \mathbf{0}_3 & \mathbf{0}_3 & \mathbf{0}_3 \\ \mathbf{0}_3 & \mathbf{0}_3 & \mathrm{I}_3 & \mathbf{0}_3 & \boldsymbol{R}_{\mathrm{IB}}^{\mathrm{T}} \\ \mathbf{0}_3 & \mathbf{0}_3 & \mathbf{0}_3 & \mathrm{I}_3 & \mathbf{0}_3 \end{pmatrix} \boldsymbol{x} \tag{20}$$

and $\tilde{\boldsymbol{\nu}}$ is a 12×1 vector of measurement noise.

[*]MTD2 model details available at https://github.com/NSL-VT/Flight-Dynamic-Models/tree/master/MTD2

C. Initialization and Tuning of Process and Measurement Covariance

The KF, EKF, and UKF were initialized and tuned using the values provided below, where the (SI) units have been suppressed for brevity. The filters are initialized such that the first twelve initial state estimates are the initial values of the aircraft state in the simulations, and the wind state is set to zero, *i.e.*,

$$\begin{aligned}\hat{\boldsymbol{x}}(t_0)_{\text{ filters}} &= [\boldsymbol{x}_{\text{P}}(t_1)_{\text{ sim}}, \boldsymbol{x}_{\Theta}(t_1)_{\text{ sim}}, \boldsymbol{x}_{\text{v}}(t_1)_{\text{ sim}}, \boldsymbol{x}_{\omega}(t_1)_{\text{ sim}}, \boldsymbol{0}_3] \\ &= [12.54, -95.66, -214.73, -0.03, 0.06, -0.25, 11.98, 2.84, 0.89, 0.005, 0.001, -0.002, \boldsymbol{0}_3]\end{aligned}$$

The input history $\boldsymbol{\delta}(t_k)$, and the measurement history $\boldsymbol{z}(t_k)$ are given by

$$\begin{aligned}\boldsymbol{\delta}(t_k : k \in \{0, 1, \ldots, N-1\})_{\text{ filters}} &= \boldsymbol{\delta}(t_k : k \in \{1, 2, \ldots, N\})_{\text{ sim}} \\ \boldsymbol{z}(t_k : k \in \{0, 1, \ldots, N-1\})_{\text{ filters}} &= \boldsymbol{y}(t_k : k \in \{1, 2, \ldots, N\})_{\text{ sim}} + \tilde{\boldsymbol{\nu}}\end{aligned}$$

where N is the number of data points collected, and $\tilde{\boldsymbol{\nu}}$ is a zero-mean Gaussian measurement noise vector with covariance matrix $\boldsymbol{R}$. The measurement noise covariance matrices in the two simulated turbulence conditions are

$$\begin{aligned}\boldsymbol{R}_{\text{filters, sim1}} &= 10^{-6} \cdot \mathbb{I}_{12} \\ \boldsymbol{R}_{\text{filters, sim2}} &= \text{diag}\left(\left[10^{-1}, 10^{-1}, 10^{-1}, 10^{-4}, 10^{-4}, 10^{-4}, 10^{-2}, 10^{-2}, 10^{-2}, 10^{-6}, 10^{-6}, 10^{-6}\right]\right)\end{aligned}$$

where "sim1" and "sim2" refer to the low and high turbulence simulation conditions, respectively. The initial state estimate error covariance matrices $\boldsymbol{P}(t_0)$ are

$$\begin{aligned}\boldsymbol{P}(t_0)_{\text{filters, sim1}} &= \begin{pmatrix} \boldsymbol{R}_{\text{filters, sim1}} & \boldsymbol{0}_{12\times 3} \\ \boldsymbol{0}_{3\times 12} & 0.01 \cdot \mathbb{I}_3 \end{pmatrix} \\ \boldsymbol{P}(t_0)_{\text{filters, sim2}} &= \begin{pmatrix} \boldsymbol{R}_{\text{filters, sim2}} & \boldsymbol{0}_{12\times 3} \\ \boldsymbol{0}_{3\times 12} & 0.01 \cdot \mathbb{I}_3 \end{pmatrix}\end{aligned}$$

The process noise covariance matrix $\boldsymbol{Q}$ of the zero-mean Gaussian process noise vector $\tilde{\boldsymbol{w}}$ for all filters is set to

$$\boldsymbol{Q}_{\text{filters}} = \begin{pmatrix} \boldsymbol{Q}_{s_{12\times 12}} & \boldsymbol{0}_{12\times 3} \\ \boldsymbol{0}_{3\times 12} & \boldsymbol{Q}_{w_{3\times 3}} \end{pmatrix}$$

where $\boldsymbol{Q}_s = 0.001 \cdot \mathbb{I}_{12}$, and $\boldsymbol{Q}_w = 0.1 \cdot \mathbb{I}_3$. The UKF parameters α, β, and κ discussed in Section IV.E were set to

$\alpha = 0.01$, $\beta = 2$, and $\kappa = 0$.

D. Example Aircraft

The flight dynamic model used here describes the motion of the My Twin Dream (MTD), an RC twin-engine, electrically powered, foam-structured, fixed-wing aircraft manufactured by My Fly Dream. The aircraft is powered by a four-cell 14.8 V 6750 mAh Lithium-polymer battery with counter-rotating twin propellers. See Figure 6. The mass and geometric properties of the MTD are shown in Table 3, and its aerodynamic parameters, as identified from flight test data, are shown in Table 4. The aerodynamic parameters obtained from flight data are uncertain. We adopt the nominal parameter values for the simulations discussed here.

Table 3 MTD aircraft properties.

Property	Symbol	Value	Units
Mass	m	3.311	kg
Mean aerodynamic chord	$\bar{c}$	0.254	m
Projected wing span	b	1.80	m
Wing planform area	S	0.457	m^2
Number of propellers	η_n	2	—
Propeller efficiency	η_e	90	%
Propeller diameter	D	0.254	m
Roll moment of inertia	I_{xx}	0.319	kg-m^2
Pitch moment of inertia	I_{yy}	0.267	kg-m^2
Yaw moment of inertia	I_{zz}	0.471	kg-m^2
Product of inertia	I_{xz}	0.024	kg-m^2

Fig. 6 My Twin Dream (MTD) aircraft.

Table 4 MTD aircraft aerodynamic parameters.

Term	$\hat{\theta} \pm \sigma$	Term	$\hat{\theta} \pm \sigma$	Term	$\hat{\theta} \pm \sigma$
C_{X_0}	+0.009 ± 0.026	C_{Z_0}	-0.255 ± 0.074	C_{m_0}	+0.008 ± 0.006
C_{X_α}	+0.282 ± 0.000	C_{Z_α}	-4.436 ± 0.015	C_{m_α}	-0.444 ± 0.027
$C_{X_{\delta e}}$	+0.051 ± 0.025	C_{Z_q}	-12.540 ± 0.030	C_{m_q}	-14.019 ± 3.363
C_{J_0}	+0.116 ± 0.000			$C_{m_{\delta e}}$	-0.415 ± 0.058
C_J	-0.040 ± 0.000				
C_{J^2}	-0.131 ± 0.000				
Term	$\hat{\theta} \pm \sigma$	Term	$\hat{\theta} \pm \sigma$	Term	$\hat{\theta} \pm \sigma$
C_{Y_β}	-0.410 ± 0.115	C_{l_β}	-0.035 ± 0.004	C_{n_β}	+0.083 ± 0.020
C_{Y_p}	+0.221 ± 0.133	C_{l_p}	-0.386 ± 0.041	C_{n_r}	-0.119 ± 0.029
C_{Y_r}	+0.230 ± 0.547	$C_{l_{\delta a}}$	-0.137 ± 0.010	$C_{n_{\delta a}}$	+0.013 ± 0.009
$C_{Y_{\delta a}}$	+0.118 ± 0.011			$C_{n_{\delta r}}$	-0.068 ± 0.006
$C_{Y_{\delta r}}$	+0.136 ± 0.030				

E. Aircraft Simulation in Turbulent Wind Field

To demonstrate KF-, EKF- and UKF-based wind estimation, we simulate the motion of the MTD in turbulent wind, using the nominal parameter values in Tables 3 and 4. We adopt the two-dimensional von Kármán turbulence model

and apply proportional feedback control, designed to keep the aircraft in straight and level, constant altitude flight. The effective flow angular velocity, represented by ω_W in Eqn. (7b), was assumed to be zero. In all simulations, the nominal airspeed is $V_t = ||v_r|| = 20$ m/s. The 2D von Kármán turbulence model is characterized by power spectral density functions of spatial frequencies Ω_1 and Ω_2. Assuming that the nominal aircraft motion is due North, the gust spectrum components in the North, East, and down directions are, respectively,

$$\Psi_{11}(\Omega_1,\Omega_2) = \frac{\sigma^2}{6\pi}(1.339L)^2\frac{1+(1.339L\Omega_1)^2+\frac{11}{3}(1.339L\Omega_2)^2}{\left[1+1.339^2L^2(\Omega_1^2+\Omega_2^2)\right]^{7/3}} \tag{21a}$$

$$\Psi_{22}(\Omega_1,\Omega_2) = \frac{\sigma^2}{6\pi}(1.339L)^2\frac{1+\frac{11}{3}(1.339L\Omega_1)^2+(1.339L\Omega_2)^2}{\left[1+1.339^2L^2(\Omega_1^2+\Omega_2^2)\right]^{7/3}} \tag{21b}$$

$$\Psi_{33}(\Omega_1,\Omega_2) = \frac{4\sigma^2}{9\pi}(1.339L)^4\frac{(\Omega_1^2+\Omega_2^2)}{[1+1.339^2L^2(\Omega_1^2+\Omega_2^2)]^{7/3}} \tag{21c}$$

where L is the turbulence length scale in feet, σ is the turbulence intensity in feet per second, and $\Omega_{1,2}$ have units of radians per foot. The simulated wind conditions were for the turbulence length scale $L = 25$ ft, turbulence intensity for the low and high turbulence simulations of $\sigma = 0.5$ and $\sigma = 25$ ft/s, respectively, and over spatial frequencies Ω_1 and Ω_2 ranging from 10^{-4} to 1 rad/ft. Motion histories from two simulations are illustrated in Figures 7a and 7b. In the first simulation, the turbulence intensity $\sigma = 0.5$ ft/s was selected to keep the wind disturbance small; see Figure 7a. In the second simulation, the turbulence intensity $\sigma = 25$ ft/s was selected so that the wind disturbance was large enough to cause significant deviations from the nominal motion; see Figure 7b.

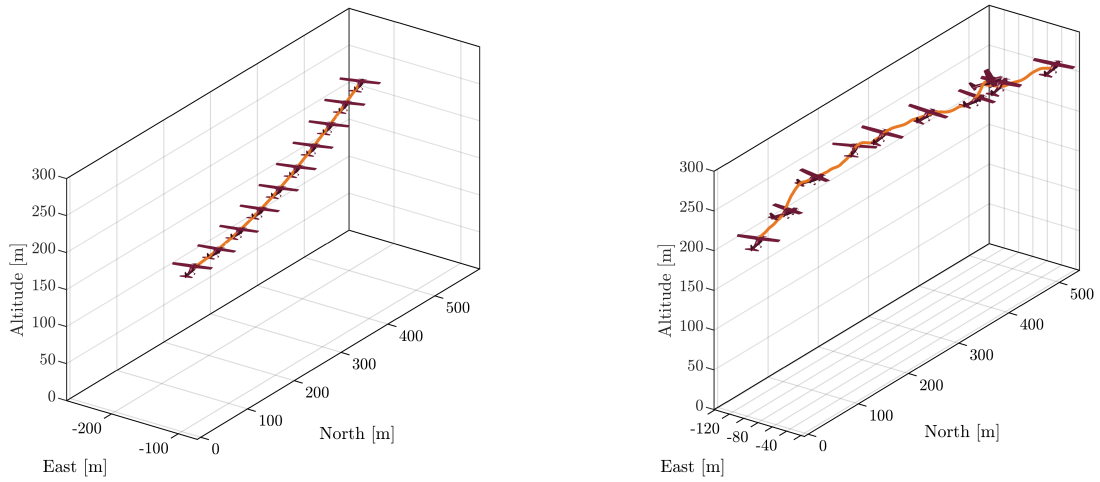

(a) **(b)**

Fig. 7 Simulated flight trajectory of the MTD aircraft subject to (a) small intensity and (b) large intensity two-dimensional von Kármán turbulence.

F. Results and Discussion

To implement KF-based wind estimation, the system (18) must be linearized about an equilibrium condition $\boldsymbol{x}^* = [\boldsymbol{P}^*, \boldsymbol{\Theta}^*, \boldsymbol{v}_{\mathrm{r}}^*, \boldsymbol{\omega}^*, \boldsymbol{V}_{\mathrm{W}}^*]\mathrm{T}$ and a nominal control input $\boldsymbol{\delta}^* = [\delta_{\mathrm{a}}, \delta_{\mathrm{e}}, \delta_{\mathrm{r}}, \delta_{\mathrm{rps}}]$. We chose the following values that correspond to steady, straight and level, constant-altitude flight:

$$\begin{aligned} \boldsymbol{x}^* &= [\mathbf{0}_{1\times 3}, 0, -0.189, -0.133, 19.36, 0, 0.33, \mathbf{0}_{1\times 6}]\mathrm{T} \\ \boldsymbol{\delta}^* &= [0, 0, 0, 220]\mathrm{T} \end{aligned} \tag{22}$$

The EKF does not require linearization about a nominal state and input, but the formulation involves recursive linearization about each state estimate in the discrete sequence, as discussed in Section IV.D. Similarly, the UKF does not require linearization about a nominal state and input, but employs a sampling approach that captures the nonlinear state distribution through a set of carefully chosen sigma points, as discussed in Section IV.E. Note that the system (18) is a continuous-time system, whereas the filter descriptions in Section IV are provided for discrete-time systems. A sampled-data implementation is used here to implement the KF, EKF, and UKF. Additionally, the nonlinear measurement model (20) is used directly to implement the EKF and UKF; the measurement equation is linearized about $\boldsymbol{x}^*$ to implement the KF.

Figures 7a and 7b show the two simulated flights for which wind estimation results obtained using the KF, EKF, and the UKF schemes are shown in Figures 8 and 9, respectively. Because the true wind velocity is known, one may also view the estimation error shown in Figures 10 and 11. These figures indicate that the three filters perform similarly, providing accurate wind estimates in the relatively benign wind field for the flight data simulated in Figure 7a. For the data in Figure 7b, the EKF and UKF-based wind estimates outperform the KF. This result is expected because the aircraft is perturbed significantly from the nominal trajectory used to obtain the linear model in the KF. While the EKF and UKF provide more accurate wind estimates than the KF in Figure 9, they have their own limitations. The EKF is sensitive to the initial state estimate error, for example, and to the process noise covariance. Incorrect initialization or a poor choice of process noise covariance matrix can cause the estimate produced by the filter to diverge. The UKF and the EKF perform similarly in providing accurate wind estimates on the simulated flight data. A possible reason for this is that the aerodynamic model used in the filter is known accurately, *i.e.*, the same aerodynamic force and moment models that were used to simulate the data were used in the filters. When these methods are implemented on experimental flight data, the identified aerodynamic model does not capture perfectly the aerodynamic forces and moments experienced by the aircraft. The EKF will be prone to error in this case as the EKF requires taking the Jacobian of the equations of motion which introduces error from linearization. The UKF does not require this linearization and instead relies on propagated sigma points, thus making the UKF less susceptible to error from model uncertainty when implementing a model-based wind estimation scheme on experimental flight data.

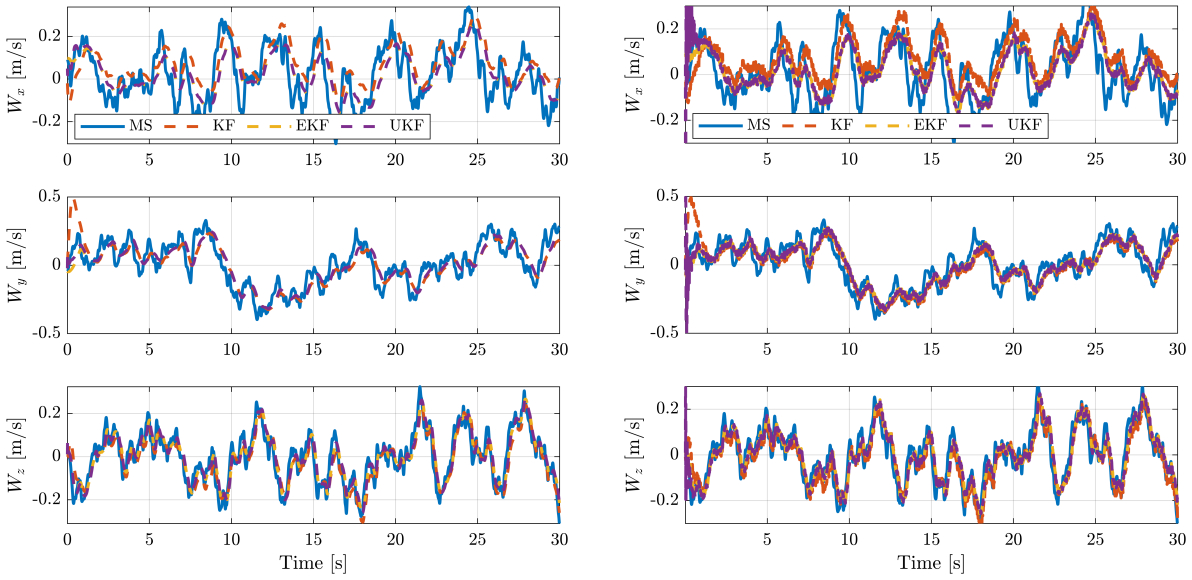

Fig. 8 Wind estimates from the simulated flight shown in Figure 7a where *MS* indicates the directly measured wind velocity (a) without and (b) with measurement noise.

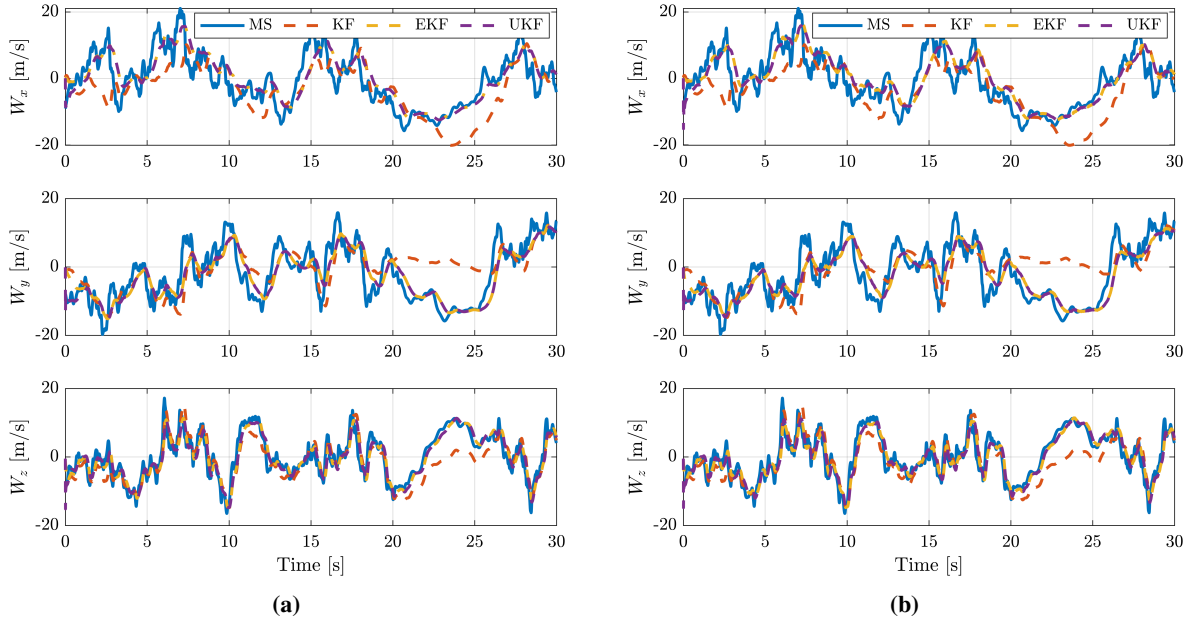

Fig. 9 Wind estimates from the simulated flight shown in Figure 7b where *MS* indicates the directly measured wind velocity (a) without and (b) with measurement noise.

VII. Conclusion

This paper presents a tutorial survey of literature on indirect wind estimation using small multirotor and fixed-wing UAVs, distinguishing between model-free and model-based methods. A general description of the wind field is provided, along with dynamic equations that approximate the motion of a UAV in wind. The paper reviews existing work on

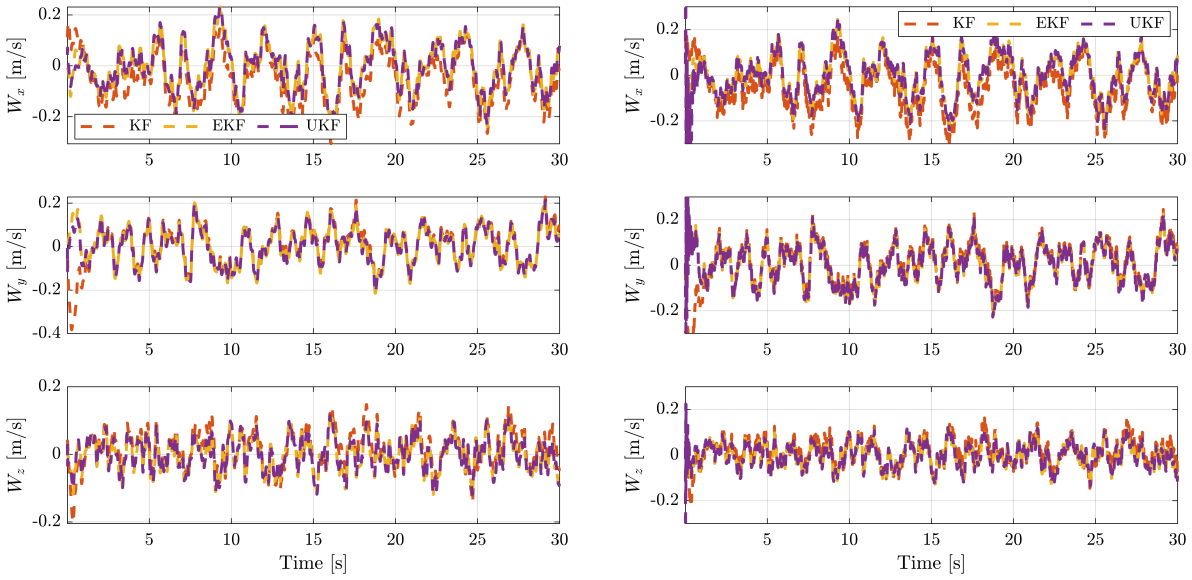

(a) (b)

Fig. 10 Wind estimate error from the simulated flight shown in Figure 7a where the measured wind velocity (a) includes or (b) does not include measurement noise.

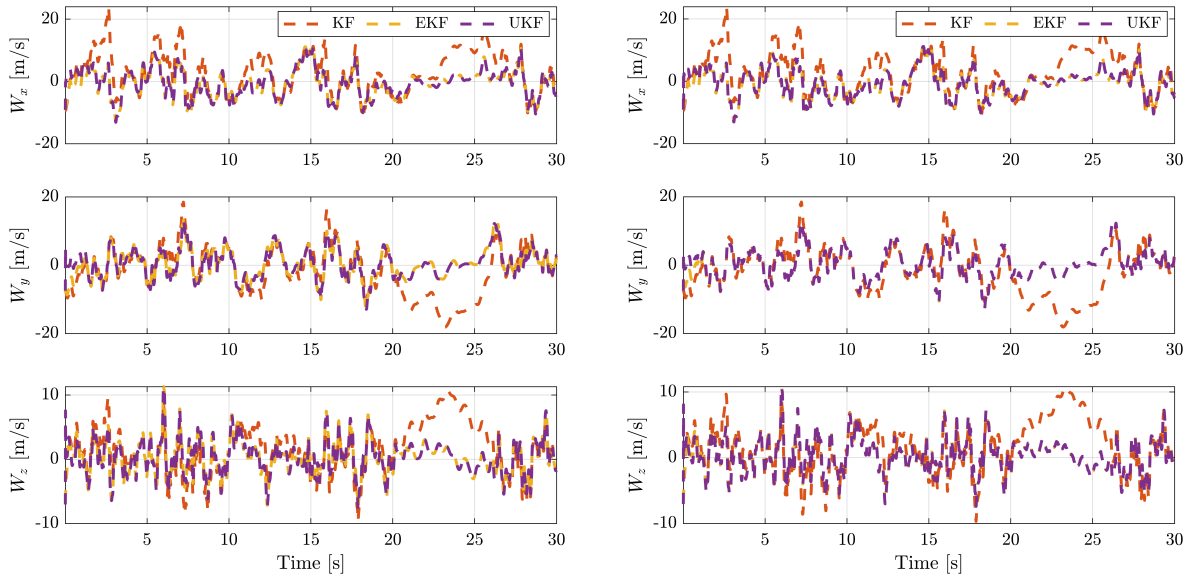

(a) (b)

Fig. 11 Wind estimate error from the simulated flight shown in Figure 7b where the measured wind velocity (a) includes or (b) does not include measurement noise.

model-based and model-free wind estimation formulations and includes a tutorial review of the more commonly used estimation algorithms. The paper describes assumptions that are commonly used when implementing a wind estimation algorithm, as well as the physical and mathematical implications of these assumptions. The survey reflects the observation that model-based wind estimation methods using a Kalman filter, extended Kalman filter, unscented

Kalman filter, or deterministic observer, for example, are more prevalent in the literature than model-free wind estimation methods. The survey closes with results of model-based wind estimation using simulated flight data for a fixed-wing UAV traversing a two-dimensional von Kármán flow field. Simulation data, for which the wind velocity is exactly known, are helpful in comparing the performance of various estimation schemes. Results for three different estimators – a Kalman filter, an extended Kalman filter, and an unscented Kalman filter – for simulated flight through two different intensities of turbulence help to illustrate the relative merits of the three approaches. The simpler Kalman filter performs comparably to the extended Kalman filter and an unscented Kalman filter in a benign wind field, while the extended Kalman filter and the unscented Kalman filter perform better under significant disturbances, provided the filter parameters and vehicle motion allow for a convergent extended state estimate. The implementation of model-based wind estimation in Section VI uses a fixed-wing aircraft model, but a multirotor model may be used as well. The aerodynamic force and moment models would need to be changed accordingly. It is expected that the wind estimation results will be similar to those shown in this paper using the Kalman filter, extended Kalman filter, and unscented Kalman filter in the two different intensities of simulated turbulence. As model-based wind estimation relies on identifying a correct model for a UAV, an area for future investigation is to understand how uncertainty in the model impacts wind velocity estimates and how to reduce the negative effects of this model uncertainty in various wind estimation schemes. Additional work in model-free wind estimation might further explore the need for persistent excitation and its implications for aircraft motion planning. Finally, future wind estimation schemes could explicitly incorporate more accurate turbulence models for the given operating environment (e.g., the atmospheric boundary layer) to improve accuracy.

Funding Sources

This work was supported by the NASA University Leadership Initiative program under Grant No. 80NSSC20M0162.

Acknowledgments

The authors gratefully acknowledge the supporting efforts of James L. Gresham and Jeremy W. Hopwood in developing the aircraft and flight dynamic model. The authors also thank Kenneth C. Gahan and the anonymous reviewers for thoughtful feedback on earlier drafts of this manuscript.

References

[1] Poikonen, S., and Campbell, J. F., "Future directions in drone routing research," *Networks*, Vol. 77, No. 1, 2021, pp. 116–126.

[2] Greenwood, W. W., Lynch, J. P., and Zekkos, D., "Applications of UAVs in civil infrastructure," *Journal of Infrastructure Systems*, Vol. 25, No. 2, 2019, p. 04019002. https://doi.org/10.1061/(ASCE)IS.1943-555X.0000464.

[3] Radoglou-Grammatikis, P., Sarigiannidis, P., Lagkas, T., and Moscholios, I., "A compilation of UAV applications for precision agriculture," *Computer Networks*, Vol. 172, 2020, p. 107148. https://doi.org/https://doi.org/10.1016/j.comnet.2020.107148.

[4] Nex, F., and Remondino, F., "UAV for 3D mapping applications: a review," *Applied Geomatics*, Vol. 6, No. 1, 2014, pp. 1–15. https://doi.org/10.1007/s12518-013-0120-x.

[5] Barbieri, L., Kral, S. T., Bailey, S. C., Frazier, A. E., Jacob, J. D., Reuder, J., Brus, D., Chilson, P. B., Crick, C., Detweiler, C., Doddi, A., Elston, J., Foroutan, H., González-Rocha, J., Greene, B. R., Guzman, M. I., Houston, A. L., Islam, A., Kemppinen, O., Lawrence, D., Pillar-Little, E. A., Ross, S. D., Sama, M. P., Schmale, D. G., Schuyler, T. J., Shankar, A., Smith, S. W., Waugh, S., Dixon, C., Borenstein, S., and Boer, G. D., "Intercomparison of small unmanned aircraft system (sUAS) measurements for atmospheric science during the LAPSE-RATE campaign," *Sensors (Switzerland)*, Vol. 19, No. 9, 2019. https://doi.org/10.3390/s19092179.

[6] Jensen, A. A., Pinto, J. O., Bailey, S. C., Sobash, R. A., Boer, G. D., Houston, A. L., Chilson, P. B., Bell, T., Romine, G., Smith, S. W., Lawrence, D. A., Dixon, C., Lundquist, J. K., Jacob, J. D., Elston, J., Wwaugh, S., and Steiner, M., "Assimilation of a coordinated fleet of uncrewed aircraft system observations in complex terrain: EnKF system design and preliminary assessment," *Monthly Weather Review*, Vol. 149, No. 5, 2021, pp. 1459–1480. https://doi.org/10.1175/MWR-D-20-0359.1.

[7] Nolan, P. J., Pinto, J., González-Rocha, J., Jensen, A., Vezzi, C. N., Bailey, S. C., de Boer, G., Diehl, C., Laurence, R., Powers, C. W., Foroutan, H., Ross, S. D., and Schmale, D. G., "Coordinated unmanned aircraft system (UAS) and ground-based weather measurements to predict Lagrangian coherent structures (LCSs)," *Sensors (Switzerland)*, Vol. 18, No. 12, 2018. https://doi.org/10.3390/s18124448.

[8] Pillar-Little, E. A., Greene, B. R., Lappin, F. M., Bell, T. M., Segales, A. R., Azevedo, G. B. H. D., Doyle, W., Kanneganti, S. T., Tripp, D. D., and Chilson, P. B., "Observations of the thermodynamic and kinematic state of the atmospheric boundary layer over the San Luis Valley, CO, using the CopterSonde 2 remotely piloted aircraft system in support of the LAPSE-RATE field campaign," *Earth System Science Data*, Vol. 13, No. 2, 2021, pp. 269–280. https://doi.org/10.5194/essd-13-269-2021.

[9] Segales, A. R., Greene, B. R., Bell, T. M., Doyle, W., Martin, J. J., Pillar-Little, E. A., and Chilson, P. B., "The CopterSonde: An insight into the development of a smart unmanned aircraft system for atmospheric boundary layer research," *Atmospheric Measurement Techniques*, Vol. 13, No. 5, 2020, pp. 2833–2848. https://doi.org/10.5194/amt-13-2833-2020.

[10] De Wekker, S. F. J., Kossmann, M., Knievel, J. C., Giovannini, L., Gutmann, E. D., and Zardi, D., "Meteorological applications benefiting from an improved understanding of atmospheric exchange processes over mountains," *Atmosphere*, Vol. 9, No. 10, 2018. https://doi.org/10.3390/atmos9100371.

[11] Kumar, A., and Ben-Tzvi, P., "Estimation of wind conditions utilizing RC helicopter dynamics," *IEEE/ASME Transactions on Mechatronics*, Vol. 24, No. 5, 2019, pp. 2293–2303. https://doi.org/10.1109/TMECH.2019.2937844.

[12] Torgesen, A. J., How, J. P., and Cameron, B., "Airborne sensing for ship air wake surveys with a tethered autonomous UAV," *AIAA Scitech 2021 Forum*, AIAA, 2021. https://doi.org/10.2514/6.2021-0381.

[13] Phelps, D., Gamagedara, K., Waldron, J., Patil, K., and Snyder, M., "Ship air wake detection using a small fixed wing unmanned aerial vehicle," *AIAA Aerospace Sciences Meeting, 2018*, AIAA, 2018. https://doi.org/10.2514/6.2018-0784.

[14] Cooper, J., S R Pappu, V., Liu, Y., and Horn, J., "Vehicle Modeling for Flight Test Measurements of Ship Airwake Disturbances," *Fourm of the American Helicopter Society*, 2016.

[15] Schafer, S., Horn, J., and Cooper, J., "Flight Test Measurement of Ship Airwake Disturbances using Small-Scale Rotorcraft," *Fourm of the American Helicopter Society*, 2015.

[16] Cooper, J., Horn, J., Yomchinda, T., and O'Neill, E., "Handling Qualities Evaluation of an Adaptive Disturbance Compensation System for Ship-Based Rotorcraft," *Journal of the American Helicopter Society*, Vol. 59, 2014. https://doi.org/10.4050/JAHS.59.022007.

[17] Benders, S., Wenz, A., and Johansen, T. A., "Adaptive path planning for unmanned aircraft using in-flight wind velocity estimation," *Proceedings of the 2018 International Conference on Unmanned Aircraft Systems*, IEEE, 2018, pp. 483–492. https://doi.org/10.1109/ICUAS.2018.8453341.

[18] Gavrilović, N., Bronz, M., and Moschetta, J.-M., "Bioinspired energy harvesting from atmospheric phenomena for small unmanned aerial vehicles," *Journal of Guidance, Control, and Dynamics*, Vol. 43, No. 4, 2020, pp. 685–699. https://doi.org/10.2514/1.G004730.

[19] Langelaan, J. W., Spletzer, J., Montella, C., and Grenestedt, J., "Wind field estimation for autonomous dynamic soaring," *Proceedings of the IEEE International Conference on Robotics and Automation*, IEEE, 2012, pp. 16–22. https://doi.org/10.1109/ICRA.2012.6224954.

[20] Cooper, J., Neal, D., De Wekker, S., Reed, A., Andrekanic, A. R., and Paulini, M. S., "Atmospheric Sampling in Urban Areas and Complex Terrain using UAS Swarms,," *Fourm of the American Helicopter Society*, 2020.

[21] "NASA Aeronautics Strategic Implementation Plan," *Aeronautics Research Mission Directorate*, 2019. URL https://www.nasa.gov/sites/default/files/atoms/files/armd-strategic-implementation-plan.pdf.

[22] Wilson, T. C., Brenner, J., Morrison, Z., Jacob, J. D., and Elbing, B. R., "Wind speed statistics from a small UAS and its sensitivity to sensor location," *Atmosphere*, Vol. 13, No. 3, 2022. https://doi.org/10.3390/atmos13030443.

[23] Tian, P., Chao, H., Rhudy, M., Gross, J., and Wu, H., "Wind sensing and estimation using small fixed-wing unmanned aerial vehicles: A survey," *Journal of Aerospace Information Systems*, Vol. 18, No. 3, 2021, pp. 132–143. https://doi.org/10.2514/1.I010885.

[24] Abichandani, P., Lobo, D., Ford, G., Bucci, D., and Kam, M., "Wind measurement and simulation techniques in multi-rotor small unmanned aerial vehicles," *IEEE Access*, 2020. https://doi.org/10.1109/ACCESS.2020.2977693.

[25] Gebre-Egziabher, D., and Gleason, S., *GNSS Applications and Methods*, Artech House, 2009, pp. 149–176.

[26] Etkin, B., *Dynamics of Atmospheric Flight*, Dover Books on Aeronautical Engineering, Dover Publications, 2005.

[27] Morelli, E. A., and Klein, V., *Aircraft System Identification: Theory and Practice*, Sunflyte Enterprises, Williamsburg, VA, 2016, Vol. 2, pp. 27–74.

[28] Kaimal, J. C., and Finnigan, J. J., *Atmospheric Boundary Layer Flows: Their Structure and Measurement*, Oxford University Press, 1994. https://doi.org/10.1093/oso/9780195062397.001.0001.

[29] Arnold, L., *Stochastic Differential Equations: Theory and Application*, Vol. 1, John Wiley & Sons, New York, 1974.

[30] Etkin, B., and Reid, L. D., *Dynamics of Flight*, Vol. 2, Wiley New York, 1995.

[31] DoD, U., *MIL-F-8785C, Military Specification Flying Qualities of Piloted Airplanes*, 1980.

[32] Thomasson, P., and Woolsey, C. A., "Vehicle motion in currents," *IEEE Journal of Oceanic Engineering*, Vol. 38, No. 2, 2013, pp. 226–242. https://doi.org/10.1109/JOE.2013.2238054.

[33] Greenwell, D., "A Review of Unsteady Aerodynamic Modelling for Flight Dynamics of Manoeuvrable Aircraft," *AIAA Atmospheric Flight Mechanics Conference and Exhibit*, 2004. https://doi.org/10.2514/6.2004-5276.

[34] Morelli, E. A., "Nonlinear Unsteady Aerodynamic Modeling using Empirical Orthogonal Functions," Tech. rep., NASA, 2021.

[35] Morelli, E. A., and Klein, V., *Aircraft System Identification: Theory and Practice*, Vol. 2, Sunflyte Enterprises Williamsburg, VA, 2016.

[36] Grauer, J. A., Morelli, E. A., and Murri, D. G., "Flight-test techniques for quantifying pitch rate and angle-of-attack rate dependencies," *Journal of Aircraft*, Vol. 54, No. 6, 2017, pp. 2367–2377. https://doi.org/10.2514/1.C034407.

[37] Simmons, B. M., McClelland, H. G., and Woolsey, C. A., "Nonlinear model identification methodology for small, fixed-wing, unmanned aircraft," *Journal of Aircraft*, Vol. 56, No. 3, 2019, pp. 1056–1067. https://doi.org/10.2514/1.C036773.

[38] Gresham, J. L., Simmons, B. M., Fahmi, J.-M. W., and Woolsey, C. A., "Remote uncorrelated pilot inputs for nonlinear aerodynamic model identification from flight data," *AIAA Aviation 2021 Forum*, 2021, p. 2792. https://doi.org/10.2514/6.2021-2792.

[39] Simmons, B. M., Gresham, J. L., and Woolsey, C. A., "Aero-propulsive modeling for propeller aircraft using flight data," *AIAA SciTech 2022 Forum*, 2022, p. 2171. https://doi.org/10.2514/1.C036773.

[40] Fay, G., "Derivation of the aerodynamic forces for the mesicopter simulation," Stanford University, USA, 2001.

[41] Hopwood, J. W., Simmons, B. M., and Woolsey, C. A., "Multirotor Flight Dynamic Models and Experiment Design for Estimation and Control," *AIAA SciTech 2024 Forum*, American Institute of Aeronautics and Astronautics, Orlando, Florida, 2024.

[42] Luenberger, D., "An introduction to observers," *IEEE Transactions on Automatic Control*, Vol. 16, No. 6, 1971, pp. 596–602. https://doi.org/10.1109/TAC.1971.1099826.

[43] González-Rocha, J., Woolsey, C. A., Sultan, C., Rose, N., and Wekker, S. F. D., "Measuring atmospheric winds from quadrotor motion," *AIAA Atmospheric Flight Mechanics Conference*, AIAA, 2017. https://doi.org/10.2514/6.2017-1189.

[44] González-Rocha, J., Woolsey, C. A., Sultan, C., and Wekker, S. F. D., "Sensing wind from quadrotor motion," *Journal of Guidance, Control, and Dynamics*, Vol. 42, No. 4, 2019, pp. 836–852. https://doi.org/10.2514/1.G003542.

[45] González-Rocha, J., Wekker, S. F. D., Ross, S. D., and Woolsey, C. A., "Wind profiling in the lower atmosphere from wind-induced perturbations to multirotor UAS," *Sensors (Switzerland)*, Vol. 20, No. 5, 2020. https://doi.org/10.3390/s20051341.

[46] Stengel, R. F., *Optimal Control and Estimation*, Dover Publications, Inc, 1994.

[47] Brogan, W. L., *Modern Control Theory*, 3rd ed., Prentice-Hall, Englewood Cliffs, NJ, 1991.

[48] Rugh, W. J., *Linear System Theory*, 2nd ed., Prentice-Hall, Upper Saddle River, N.J., 1996.

[49] Bar-Shalom, Y., Rong Li, X., and Kirubarajan, T., *Estimation with Applications to Tracking and Navigation*, John Wiley & Sons, 2002. https://doi.org/https://doi.org/10.1002/0471221279.

[50] Balmer, G., Muskardin, T., Wlach, S., and Kondak, K., "Enhancing model-free wind estimation for fixed-wing UAV," *2018 International Conference on Unmanned Aircraft Systems*, IEEE, 2018, pp. 1242–1247. https://doi.org/10.1109/ICUAS.2018.8453419.

[51] Hattenberger, G., Bronz, M., and Condomines, J. P., "Estimating wind using a quadrotor," *International Journal of Micro Air Vehicles*, Vol. 14, 2022. https://doi.org/10.1177/17568293211070824.

[52] Xiang, X., Wang, Z., Mo, Z., Chen, G., Pham, K., and Blasch, E., "Wind field estimation through autonomous quadcopter avionics," *AIAA/IEEE Digital Avionics Systems Conference - Proceedings*, Vol. 2016-December, IEEE, 2016. https://doi.org/10.1109/DASC.2016.7778071.

[53] Petrich, J., and Subbarao, K., "On-board wind speed estimation for UAVs," *AIAA Guidance, Navigation, and Control Conference*, AIAA, 2011. https://doi.org/10.2514/6.2011-6223.

[54] Wenz, A., Johansen, T. A., and Cristofaro, A., "Combining model-free and model-based angle of attack estimation for small fixed-wing UAVs using a standard sensor suite," *Proceedings of the 2016 International Conference on Unmanned Aircraft Systems*, IEEE, 2016, pp. 624–632. https://doi.org/10.1109/ICUAS.2016.7502583.

[55] Chen, H., Bai, H., and Taylor, C. N., "Invariant-EKF design for quadcopter wind estimation," *Proceedings of the 2022 American Control Conference (ACC)*, IEEE, 2022, pp. 1236–1241. https://doi.org/10.23919/ACC53348.2022.9867417.

[56] Cho, A. M., Kim, J., Lee, S., and Kee, C., "Wind estimation and airspeed calibration using a UAV with a single-antenna GPS receiver and pitot tube," *IEEE Transactions on Aerospace and Electronic Systems*, Vol. 47, No. 1, 2011. https://doi.org/10.1109/TAES.2011.5705663.

[57] Lie, F. A. P., and Gebre-Egziabher, D., "Synthetic air data system," *Journal of Aircraft*, Vol. 50, No. 4, 2013, pp. 1234–1249. https://doi.org/10.2514/1.C032177.

[58] Sun, J., Li, B., Wen, C. Y., and Chen, C. K., "Model-aided wind estimation method for a tail-sitter aircraft," *IEEE Transactions on Aerospace and Electronic Systems*, Vol. 56, No. 2, 2020, pp. 1262–1278. https://doi.org/10.1109/TAES.2019.2929379.

[59] Tian, P., and Chao, H., "Model aided estimation of angle of attack, sideslip angle, and 3D wind without flow angle measurements," *AIAA Guidance, Navigation, and Control Conference*, Vol. 0, American Institute of Aeronautics and Astronautics Inc, AIAA, 2018. https://doi.org/10.2514/6.2018-1844.

[60] Zhang, Q., Xu, Y., Wang, X., Yu, Z., and Deng, T., "Real-time wind field estimation and pitot tube calibration using an extended kalman filter," *Mathematics*, Vol. 9, No. 6, 2021. https://doi.org/10.3390/math9060646.

[61] Julier, S. J., and Uhlmann, J. K., "New extension of the Kalman filter to nonlinear systems," *Signal Processing, Sensor Fusion, and Target Recognition VI*, Vol. 3068, edited by I. Kadar, International Society for Optics and Photonics, SPIE, 1997, pp. 182 – 193. https://doi.org/10.1117/12.280797.

[62] Rhudy, M. B., Gu, Y., and Chao, H., "Wind field velocity and acceleration estimation using a small UAV," *Proceedings of the AIAA Modeling and Simulation Technologies Conference*, AIAA, 2014. https://doi.org/10.2514/6.2014-2647.

[63] Wan, E., and Van Der Merwe, R., "The unscented Kalman filter for nonlinear estimation," *Proceedings of the IEEE 2000 Adaptive Systems for Signal Processing, Communications, and Control Symposium (Cat. No.00EX373)*, 2000, pp. 153–158. https://doi.org/10.1109/ASSPCC.2000.882463.

[64] Condomines, J.-P., Bronz, M., Hattenberger, G., and Erdelyi, J.-F., "Experimental wind field estimation and aircraft identification," *IMAV 2015: International Micro Air Vehicles Conference and Flight Competition*, 2015.

[65] Larrabee, T., Chao, H., Rhudy, M., Gu, Y., and Napolitano, M. R., "Wind field estimation in UAV formation flight," *Proceedings of the American Control Conference*, IEEE, 2014, pp. 5408–5413. https://doi.org/10.1109/ACC.2014.6859266.

[66] Lee, J. H., Sevil, H. E., Dogan, A., and Hullender, D., "Estimation of maneuvering aircraft states and time-varying wind with turbulence," *Aerospace Science and Technology*, Vol. 31, No. 1, 2013, pp. 87–98. https://doi.org/10.1016/j.ast.2013.09.009.

[67] Rhudy, M. B., Gu, Y., Gross, J. N., and Chao, H., "Onboard wind velocity estimation comparison for unmanned aircraft systems," *IEEE Transactions on Aerospace and Electronic Systems*, Vol. 53, No. 1, 2017, pp. 55–66. https://doi.org/10.1109/TAES.2017.2649218.

[68] Rhudy, M., Gross, J., and Gu, Y., "Stochastic wind modeling and estimation for unmanned aircraft systems," *AIAA Aviation 2019 Forum*, AIAA, 2019, pp. 1–9. https://doi.org/10.2514/6.2019-3111.

[69] Gahan, K., Hopwood, J. W., and Woolsey, C. A., "Wind estimation using an H∞ filter with fixed-wing aircraft flight test results," *AIAA SCITECH 2023 Forum*, 2023. https://doi.org/10.2514/6.2023-2252.

[70] Wenz, A., and Johansen, T. A., "Moving horizon estimation of air data parameters for UAVs," *IEEE Transactions on Aerospace and Electronic Systems*, Vol. 56, No. 3, 2020, pp. 2101–2121. https://doi.org/10.1109/TAES.2019.2946677.

[71] Kaimal, J. C., Wyngaard, J. C., Izumi, Y., and Coté, O. R., "Spectral characteristics of surface-layer turbulence," *Quarterly Journal of the Royal Meteorological Society*, Vol. 98, No. 417, 1972, pp. 563–589. https://doi.org/https://doi.org/10.1002/qj.49709841707.

[72] Mann, J., "The spatial structure of neutral atmospheric surface-layer turbulence," *Journal of Fluid Mechanics*, Vol. 273, 1994, p. 141–168. https://doi.org/10.1017/S0022112094001886.

[73] Berg, J., Natarajan, A., Mann, J., and Patton, E. G., "Gaussian vs non-Gaussian turbulence: impact on wind turbine loads," *Wind Energy*, Vol. 19, No. 11, 2016, pp. 1975–1989. https://doi.org/https://doi.org/10.1002/we.1963.

[74] Halefom, M. H., Gresham, J. L., and Woolsey, C. A., "Wind estimation from an unsteady aerodynamic fixed-wing motion model," *AIAA SciTech Forum 2022*, AIAA, 2022. https://doi.org/10.2514/6.2022-0554.

[75] Halefom, Mekonen H and Hopwwod, Jeremy W and Woolsey, Craig A, "Unsteady Aerodynamics in Model-Based Wind Estimation from Small, Fixed-Wing Aircraft Motion," *Journal of Guidance, Control, and Dynamics*, 2024 (To appear.).

[76] Hong, H., Wang, M., Holzapfel, F., and Tang, S., "Wind estimation for fixed-wing aircraft using command tracking approach," *MED 2018 - 26th Mediterranean Conference on Control and Automation*, Institute of Electrical and Electronics Engineers Inc., 2018, pp. 879–884. https://doi.org/10.1109/MED.2018.8443055.

[77] Hong, H., Wang, M., Holzapfel, F., and Tang, S., "Fast real-time three-dimensional wind estimation for fixed-wing aircraft," *Aerospace Science and Technology*, Vol. 69, 2017, pp. 674–685. https://doi.org/10.1016/j.ast.2017.07.019.

[78] Palomaki, R. T., Rose, N. T., van den Bossche, M., Sherman, T. J., and Wekker, S. F. D., "Wind estimation in the lower atmosphere using multirotor aircraft," *Journal of Atmospheric and Oceanic Technology*, Vol. 34, No. 5, 2017, pp. 1183–1191. https://doi.org/10.1175/JTECH-D-16-0177.1.

[79] Neumann, P. P., and Bartholmai, M., "Real-time wind estimation on a micro unmanned aerial vehicle using its inertial measurement unit," *Sensors and Actuators, A: Physical*, Vol. 235, 2015, pp. 300–310. https://doi.org/10.1016/j.sna.2015.09.036.

[80] Shelekhov, A., Afanasiev, A., Shelekhova, E., Kobzev, A., Tel'minov, A., Molchunov, A., and Poplevina, O., "High-Resolution Profiling of Atmospheric Turbulence Using UAV Autopilot Data," *Drones*, Vol. 7, 2023, p. 412. https://doi.org/10.3390/drones7070412.

[81] Pappu, V. S. R., Liu, Y., Horn, J. F., and Cooper, J., "Wind gust estimation on a small VTOL UAV," American Helicopter Society, Mesa, AZ, USA, 2017.

[82] Cooper, J., Hopwood, J., Woolsey, C., Wekker, S. D., and DeVore, M., "Intelligent wind estimation for chemical source localization," *VFS International 79th Annual Forum and Technology Display*, Vertical Flight Society, 2023.

[83] Velasco-Carrau, J., García-Nieto, S., Salcedo, J. V., and Bishop, R. H., "Multi-objective optimization for wind estimation and aircraft model identification," *Journal of Guidance, Control, and Dynamics*, Vol. 39, No. 2, 2016, pp. 372–389. https://doi.org/10.2514/1.G001294.

[84] Asignacion, A., Suzuki, S., Noda, R., Nakata, T., and Liu, H., "Frequency-based wind gust estimation for quadrotors using a nonlinear disturbance observer," *IEEE Robotics and Automation Letters*, Vol. 7, No. 4, 2022, pp. 9224–9231. https://doi.org/10.1109/LRA.2022.3190073.

[85] Azid, S. I., Kumar, K., Cirrincione, M., and Fagiolini, A., "Wind gust estimation for precise quasi-hovering control of quadrotor aircraft," *Control Engineering Practice*, Vol. 116, 2021. https://doi.org/10.1016/j.conengprac.2021.104930.

[86] Langelaan, J. W., Alley, N., and Neidhoefer, J., "Wind field estimation for small unmanned aerial vehicles," *Journal of Guidance, Control, and Dynamics*, Vol. 34, No. 4, 2011, pp. 1016–1030. https://doi.org/10.2514/1.52532.

[87] Marinescu, M., Olivares, A., Staffetti, E., and Sun, J., "On the estimation of vector wind profiles using aircraft-derived data and Gaussian process regression," *Aerospace*, Vol. 9, No. 7, 2022. https://doi.org/10.3390/aerospace9070377.

[88] Perozzi, G., Efimov, D., Biannic, J. M., and Planckaert, L., "Using a quadrotor as wind sensor: time-varying parameter estimation algorithms," *International Journal of Control*, Vol. 95, No. 1, 2022, pp. 126–137. https://doi.org/10.1080/00207179.2020.1780324.

[89] Rautenberg, A., Graf, M. S., Wildmann, N., Platis, A., and Bange, J., "Reviewing wind measurement approaches for fixed-wing unmanned aircraft," *Atmosphere*, Vol. 9, No. 11, 2018. https://doi.org/10.3390/atmos9110422.

[90] Witte, B. M., Singler, R. F., and Bailey, S. C., "Development of an unmanned aerial vehicle for the measurement of turbulence in the atmospheric boundary layer," *Atmosphere*, Vol. 8, No. 10, 2017. https://doi.org/10.3390/atmos8100195.

[91] Borup, K. T., Fossen, T. I., and Johansen, T. A., "A nonlinear model-based wind velocity observer for unmanned aerial vehicles," *IFAC-PapersOnLine*, Vol. 49, Elsevier B.V., 2016, pp. 276–283. https://doi.org/10.1016/j.ifacol.2016.10.177.

[92] Meier, K., Hann, R., Skaloud, J., and Garreau, A., "Wind estimation with multirotor UAVs," *Atmosphere*, Vol. 13, No. 4, 2022. https://doi.org/10.3390/atmos13040551.

[93] Salazar, L. R., Cobano, J. A., and Ollero, A., "Small UAS-based wind feature identification system Part 1: Integration and validation," *Sensors (Switzerland)*, Vol. 17, No. 1, 2017. https://doi.org/10.3390/s17010008.